# Seismicity rate immediately before and after mainshock rupture from high-frequency waveforms in Japan

Zhigang Peng, John E. Vidale, Miaki Ishii, A. Helmstetter

# Seismicity rate immediately before and after mainshock rupture from high-frequency waveforms in Japan

Zhigang Peng[1,2], John E. Vidale[1], Miaki Ishii[3], Agnes Helmstetter[4]

1. Department of Earth & Space Sciences, University of California, Los Angeles, CA, 90095-1567, USA
2. Now at School of Earth and Atmospheric Sciences, Georgia Institute of Technology, Atlanta, GA, 30332
3. Department of Earth and Planetary Sciences, Harvard University, Cambridge, MA, 02138, USA
4. Observatoire des Sciences de l'Univers de Grenoble, Laboratoire de Geophysique Interne et Tectonophysique, BP 53 Grenoble Cedex 9 38041, France

Running Title: Seismicity rate before/after mainshock

Received xx/xx/2006; revised xx/xx/2006; accepted xx/xx/2006; published xx/xx/2006.

Submitted to JGR on 03/12/2006, Revised on 09/17/2006

*Abstract*. We analyze seismicity rate immediately before and after 82 mainshocks with the magnitudes ranging from 3 to 5 using waveforms recorded by the Hi-net borehole array in Japan. By scrutinizing high-frequency signals, we detect ~5 times as many aftershocks in the first 200 s as in the Japan Meteorological Agency catalogue. After correcting for the changing completeness level immediately after the mainshock, the aftershock rate shows a crossover from a slower decay with an Omori's law exponent $p = 0.58 \pm 0.08$ between 20 and 900 s after the mainshock, to a faster decay with $p = 0.92 \pm 0.04$ after 900 s. The foreshock seismicity rate follows an inverse Omori's law with $p = 0.73 \pm 0.07$ from several tens of days up to several hundred seconds before the mainshock. The seismicity rate in the 200 s immediately before the mainshock appears steady with $p = 0.36 \pm 0.45$. These observations can be explained by the epidemic-type aftershock sequence (ETAS) model, and the rate-and-state model for a heterogeneous stress field on the mainshock rupture plane. Alternatively, non-seismic stress changes near the source region, such as episodic aseismic slip, or pore fluid pressure fluctuations, may be invoked to explain the observation of small $p$ values immediately before and after the mainshock.

Keywords: earthquake interaction, seismicity, Omori law

## 1. Introduction

Large shallow earthquakes are typically followed by increased seismic activity, known as "aftershocks", that diminish in rate approximately as the inverse of the elapsed time since the mainshock [*Omori*, 1894]. The aftershock decay rate $R(t)$ is well described by the modified Omori's Law [*Utsu et al.*, 1995]

$$R(t) = \frac{K}{(t+c)^p} \tag{1}$$

where $t$ is the time elapsed since the mainshock, and $K$, $p$, $c$ are empirical parameters. In addition, earthquakes are sometimes preceded by statistically accelerating seismic activity, known as "foreshocks" [*Jones and Molnar,* 1979; *Abercrombie and Mori*, 1996]. Recent studies have shown that the increased rate of foreshocks can be described by an inverse power law with the same functional form as the modified Omori's law for aftershocks, but the values of the parameters are different [*Jones and Molnar*, 1979; *Maeda*, 1999; *Helmstetter and Sornette*, 2003].

Among the three parameters in the modified Omori's law, the $K$ value describes aftershock productivity, which scales with mainshock magnitude $m$ [*Felzer et al.*, 2004; *Helmstetter et al.*, 2005], and depends on the cutoff magnitude of the events considered as aftershocks. Observed value for the exponent $p$ is, in general, around 1.0 [e.g., *Reasenberg and Jones*, 1989, 1994; *Utsu et al.*, 1995], although it varies for different aftershock sequences [*Wiemer and Katsumata*, 1999]. The variation in the $p$ value has been related to crustal temperature

[*Mogi*, 1962], heat flow [*Kisslinger and Jones*, 1991], degree of heterogeneity in the fault zone [*Mikumo and Miyatake*, 1979], and fractal dimension of the pre-existing fault system [*Nanjo et al.*, 1998]. However, it is still not clear which factors play the major roles in controlling the *p* value. The parameter *c* is an apparent time offset, commonly a fraction of an hour or a day. It eliminates the singularity in the aftershock rate at zero time.

The *c* value is a controversial quantity [e.g., *Utsu et al.*, 1995; *Kisslinger*, 1996]. Although it is claimed to scale with the mainshock magnitude and the lower magnitude cutoff for different aftershock sequences [*Shcherbakov et al.*, 2004], and the recurrence time of the mainshock [*Narteau et al.*, 2002], the commonly accepted view is that the *c* value is an artifact due to incompleteness of early aftershocks in a catalogue [*Kagan*, 2004; *Kagan and Houston*, 2005; *Lolli and Gasperini*, 2006]. Immediately after a large earthquake, many aftershocks are missing in the catalogue due to coda from the mainshock, and overload of processing facilities [*Kagan*, 2004]. Thus, the characteristics of the aftershock decay rate immediately after a mainshock have remained uncertain. Yet this period holds valuable information on the transition from mainshock to aftershocks, and the underlying earthquake physics that control the time-dependent behavior of aftershocks. The short-term property of aftershock decay rate is also very important for evaluating and forecasting short-term earthquake probability [*Kagan*, 2004; *Gerstenberger et al.*, 2005; *Helmstetter et al.*, 2006].

In comparison, foreshocks are less affected by catalogue incompleteness. However, only a few studies have focused on the foreshock behavior on the time scale of seconds to minutes before the mainshock [e.g., *Maeda*, 1999; *McGuire*, 2003; *McGuire et al.*, 2005]. This is because the total number of foreshocks observed is smaller than the number of aftershocks.

Often, no foreshock is observed before a mainshock. Thus, it is difficult to examine the behavior of foreshock activity based on just a few earthquake sequences. To overcome such difficulty, a stacking method is generally applied to obtain a statistical space-time distribution of foreshocks, with the assumption that every mainshock has a similar behavior of foreshock activity [*Jones and Molnar*, 1979; *Maeda*, 1999; *Reasenberg*, 1999; *Helmstetter and Sornette*, 2003]. A clearer understanding of the foreshock behavior would provide keys to a better understanding of the physical mechanism of foreshock occurrence, and may also allow us to distinguish foreshock activity from fluctuations of background seismicity, which may be useful in predicting large earthquakes [*Geller et al.*, 1997; *Chen et al.*, 1999].

More complete catalogues are needed for a better constraint on the seismicity rate immediately before and after mainshocks. An effective approach is to go beyond conventional catalogues and analyze continuous waveforms recorded by high-quality seismic stations close to the mainshock [*Vidale et al.*, 2003; *Enescu et al.*, 2006; *Peng et al.*, 2006]. For example, *Vidale et al.* [2003] have found several times more aftershocks in the first few minutes than are reported in existing catalogues from high-pass filtered seismograms for several moderate to large mainshocks in California and Japan. Unfortunately, unclipped broadband recordings from stations close to large earthquakes (e.g., $m \geq 6$) are rare. The seismicity rate immediately after a large earthquake is likely to be very high, which may cause overlapping phase arrivals, making identification of individual aftershocks difficult. Furthermore, the analysis is complicated by a relatively long mainshock rupture, and a broad spatial distribution of aftershocks. Therefore, it is difficult to assign magnitudes to aftershocks identified by a single or a few nearby stations, and assess the completeness of the catalogue in terms of event time

and minimum magnitude. On the other hand, small earthquakes (e.g., $m \leq 3$) typically have small number of aftershocks. This implies that a large number of mainshocks are required to accumulate enough aftershocks for statistically significant conclusions. Avoiding these two cases, we use waveforms from many moderate-size earthquakes (e.g., $3 \leq m \leq 5$) recorded continuously by high-quality seismometers to investigate seismic activities immediately before and after mainshocks.

In this study, we analyze waveforms of 82 earthquakes with $3 \leq m \leq 5$ that are recorded by the High Sensitivity Seismograph Network (Hi-net) in Japan [*Okada et al.*, 2004]. The Hi-net array consists of ~700 stations (Figure 1). Most of them are installed in boreholes at a depth of 100 to 300 m. Each station consists of a three-component velocity seismometer with a natural frequency of 1 Hz and a sampling rate of 100/s. In the following Sections 2 and 3, we first describe the data set and the analysis procedure. We summarize the results in Section 4. The interpretation is given in Section 5.

## 2. Data

We systematically searched the Japan Meteorological Agency (JMA) catalogue during an 18-month period (2003/12/01–2005/06/20), for shallow earthquakes in the magnitude range $3 \leq m \leq 5$, and within the rectangular area with longitude between 129°E and 146°E, and latitude between 30°N and 46°N. We then examined the waveform data that are recorded by the closest 10 stations in the Hi-net array starting ~200 s before until ~900 s after each mainshock.

To control the data quality, the following criteria are applied to select a subset of

earthquake sequences for analysis. First, we require that the best recording station in the Hi-net array be within 30 km of the mainshock epicenter. The best station, which is typically the nearest station, is defined as the one with the combination of a low pre-event noise level, a high signal-to-noise ratio, and a fast decaying mainshock coda. The distance criterion is applied to minimize the duration of the mainshock coda, which falls off with time more rapidly at closer distance. Only crustal events with hypocentral depths less than 30 km are analyzed in this study, because they are closer to the nearest station and tend to have more aftershocks than deeper events [*Kagan*, 1991; *Mori and Abercrombie*, 1997]. On the other hand, events with hypocentral depth less than 2 km are mostly associated with volcanic activities, and their behavior has been asserted to differ from that of tectonic earthquakes. So only events with their hypocentral depths within 2-30 km are included in the analysis. We also require that at least one event with $m \leq 1.5$ be present in the JMA catalogue within the time period of the retrieved waveform for magnitude calibration. The detailed calibration procedure is given in Section 3.

Finally, we select as mainshocks those earthquakes that were not preceded by large events with $m \geq 3$ by at least $R$ km and 100 days. The purpose of this selection criterion is to ensure that our mainshocks are not influenced by, or a direct consequence of, previous large events. The spatial influence length $R$ is defined as 2 times the rupture length $L(m) = 0.01 \times 10^{0.5m}$ (km) [*Working Group on California Earthquake Probabilities,* 2003] of an earthquake with magnitude $m$. The minimum value of $R$ is set to be 3 km. In addition, we eliminated one sequence that showed strong swarm-like behavior [*Vidale and Shearer*, 2006].

We then select all events within 100 days of a mainshock as aftershock sequences (Figure

2). The 100-day time window represents a compromise between a need for a sufficiently long window to accurately estimate the long-term aftershock rate, and a need to minimize the contamination from background seismicity. The spatial window for aftershocks is defined as a circle around the mainshock epicenter, with the radius equal to one-rupture length $L(m)$ + 1 km horizontal location error. We also require the depth of aftershocks to be within one-rupture length $L(m)$ + 2 km vertical location error (Figure 2).Foreshocks are defined as all events within 545 days (as limited by the availability of the JMA catalogue) before the mainshock within the same area.

As described before, we only require that a mainshock not be preceded by another event that is potentially a mainshock itself. We do not require that aftershocks be smaller than the mainshock. We believe that our selection process does not impose *a priori* assumption on the temporal variation of seismicity rate around a mainshock, but help to identify those sequences with high data quality. After the selection process, we obtain 82 events. Their hypocentral locations are widely distributed across the Japanese Islands (Figure 1).

## 3. Analysis Procedure

The three-component seismograms recorded by the best station are high-pass filtered using a two-pass Butterworth filter with a corner frequency of 30 Hz. Next, we compute the envelopes of the high-pass-filtered seismograms, stack the three-component envelopes, take the logarithm, and smooth the resulting envelope by a median operator with a half-width of 0.1 s. All procedures are done using subroutines in the Seismic Analysis Code [*Goldstein et al.*, 2003]. The results are similar for 10 to 30 Hz high-pass filters, but the data filtered with

higher frequency have sharper onsets and coda that decay more rapidly. *P*-wave arrivals are clearer on the vertical component, but we include the two horizontal components to produce a flat background noise level, and also to minimize disturbances that sometimes appear only on one channel.

We identify an event by searching for clear double peaks in the envelope that correspond to the *P* and *S* arrivals. The arrival time of the larger of the two peaks is used as a proxy for the origin time of the corresponding event, and the peak amplitude is used to estimate the event magnitude. An example is shown in Figure 3 for an $m$ = 4.1 event. The event location is shown in Figure 2. We note that delays of a few seconds exist between the high-frequency peaks (red circles) in the envelope and the actual origin time of an event given in the JMA catalogue (green stars). However, such delays are not relevant in this study when the timing of the events are measured with respect to the high-frequency peak of the mainshock. During the identification process, we check that the *S*–*P* time of each handpicked event is close to that of the mainshock. This ensures that the events are located near the mainshock. We also examine the high-pass-filtered envelopes of the nearby stations to confirm that large events are recorded by other stations besides the best one. Finally, the amplitude immediately before each event is used as a measure for the pre-event noise level. Only events with peak amplitude at least 0.3 (in logarithmic scale) larger than the noise level (i.e., a signal-to-noise ratio of ~2) are retained for further analysis.

Assuming that a 10-fold increase in amplitude corresponds to an increase in one-unit of magnitude, we estimate the magnitude of each handpicked event using its peak amplitude. First, we use events that are both identified by our procedure and are listed in the JMA

catalogue to calibrate an amplitude-magnitude relation. This is done by shifting the envelope function so that the logarithmic amplitudes match the magnitudes of small events listed in the JMA catalogue. Only events small enough with their corner frequencies above 30 Hz are used for such calibration. If we assume a circular crack model [*Eshelby*, 1957] and a stress drop of 3 MPa, the corner frequency of an event with $m$ = 1.5 is about 30 Hz. So we use $m < 1.5$ to calibrate the amplitude-magnitude relation in this study. As shown in Figure 4, the magnitudes estimated from the envelope amplitudes match well with the JMA magnitudes for small events. We underestimate magnitudes of events larger than 1.5, because 30 Hz is above their corner frequencies. We derive an empirical relation of $m_{JMA} = (m_{AMP} - 1.5) \times 1.6 + 1.5$ ($m_{AMP} \geq 1.5$), and $m_{JMA} = m_{AMP} \times 1.0$ ($m_{AMP} < 1.5$) from a least-squares fitting (Figure 4), and apply it for magnitude correction, where $m_{JMA}$ denotes the JMA magnitude, and $m_{AMP}$ is the magnitude from the envelope amplitude.

We then combine the handpicked events (e.g., Figure 3) with those listed in the JMA catalogue into one catalogue for each sequence (e.g., Figure 5). For consistency, we use the origin times and magnitudes determined from the envelopes for events in the time range of [–200, 900] s relative to the mainshock origin time. For those events that are outside this time window, we use the origin times and magnitudes listed in the JMA catalogue. Finally, we examine all 82 sequences together for both foreshocks and aftershocks.

## 4. Results

### 4.1 General features

The stacked aftershock sequences (Figure 6a) show several interesting features. First, we

have detected 5 times as many aftershocks in the first 200 s with $m \geq 0$ as are listed in the JMA catalogue. This indicates that our procedure is more effective in identifying early aftershocks than the conventional methods employed by the JMA. Figure 7 shows the fraction of events listed in the JMA catalogue and identified by our handpicking procedure in each logarithmic time bins. As expected, the fraction of detected events in the conventional catalogue increases with an increase in cutoff magnitude and time elapsed since the mainshock [*Kagan*, 2004; *Helmstetter et al.*, 2006]. We note that some small events are still missing in the JMA catalogue at 900 s after the mainshock.

The change in detection threshold with time and magnitude is also evident for our handpicked events. This indicates that our handpicked catalogue is probably incomplete at early times, just like the JMA catalogue. That is, small events escape detection if their amplitudes are below these of the codas of the mainshock or large aftershocks [*Kagan*, 2004; *Kilb et al.*, 2004]. The completeness of our handpicked catalogue within the first 900 s is quantified in the next section. We return to examining the seismicity rate around the mainshocks in Section 4.3.

Figure 6a show that the density (number of events per unit log time) of events becomes greater at all magnitude levels as time passes. Because the horizontal axis is in logarithm of time, a constant density of events indicates that the seismicity rate decays with $1/t$, which means $p = 1$. Thus, an increase in density at all magnitude levels suggests that the $p$ value is less than 1, especially at times immediately after the mainshock.

The stacked foreshock sequences shown in Figure 6b are more scattered than the aftershock sequences. The log-scale densities for both foreshocks and aftershocks are

comparable at several tens of days away from the mainshock occurrence time. Since foreshocks occur before the mainshocks, they are relatively free of the incompleteness caused by the mainshock coda. Indeed, we observe two immediate foreshocks within 10 s before the mainshock. However, there is a clear lack of small foreshocks in the last 20 s before the mainshock.

### 4.2 Catalogue completeness

The catalogue completeness is often discussed in terms of magnitude threshold (or cutoff) $m_c$, the magnitude above which all events are identified in the catalogue. A standard way of estimating $m_c$ is to find the minimum magnitude that fits the *Gutenberg and Richter* [1944] (G-R) frequency-magnitude relation. Based on the assumption of self-similarity, *Wiemer and Wyss* [2000] proposed to estimate $m_c$ using the point of the maximum curvature (MAXC) for the non-cumulative frequency-magnitude distribution. Since aftershocks listed in the JMA catalogue are not complete in the first few hundred seconds (Figure 7), we use aftershocks between 2000 s and 100 days to compute a non-cumulative frequency-magnitude distribution. The number of aftershocks is peaked at $m$ = 0.7 (Figure 8a). *Woessner and Wiemer* [2005] have found that $m_c$ values obtained from the MAXC method is typically 0.1-0.2 smaller than those from other methods. However, as will be shown in Figure 10, our results do not vary significantly with the $m_c$ value. . So we obtain $m_c$ = 0.7 and a $b$ value of 0.81 using the discrete Gutenberg-Richter model of *Utsu* [1966], with magnitude bins of width $dm$ = 0.1 for the JMA catalogue.

Since the maximum curvature for the non-cumulative frequency-magnitude distribution of

the handpicked events is not well defined, it is difficult to estimate their $m_c$ and the $b$ values even at several hundred seconds after the mainshock (Figure 8b). In addition, we only have ~300 aftershocks in the first 100 s after the mainshock when the $m_c$ is changing dramatically with time (Figure 8c). Since the maximum curvature method typically requires several hundred events in each space-time window for statistically significant result, this method cannot provide an accurate estimation of $m_c$ in the first 100 s [*Kagan*, 2004]. Recently, *Helmstetter et al.* (2006) have proposed an empirical relation for $m_c$ as a function of the mainshock magnitude and the elapsed time. However, that relationship is based on several large ($m \geq 6$) aftershock sequences in southern California. Thus, the applicability of this relationship to the 82 sequences in Japan with smaller mainshock magnitude is not clear.

Incomplete detection of small aftershocks is inevitable due to coda of the mainshock and large aftershocks immediately after the mainshock [*Kagan*, 2004]. The amplitudes and durations of coda waves depend not only on the mainshock magnitude, but also on the hypocentral distance, the heterogeneity of the crust, and near-station structures [e.g., *Aki*, 1969; *Sato and Fehler*, 1998]. Thus, different aftershock sequences are expected to have different coda durations, and hence different magnitude detection thresholds.

To treat each sequence separately, we use the envelope amplitude right before each event (the noise level discussed in Section 2) + 0.3 as a measure of the local $m_c$ at the time of that event. In addition, we compute $m_{c95}(t)$, the magnitude below which 95% of the $m_c$ values exist as a function of time, and use it as a measure of the completeness for the stacked aftershock sequences. The $m_{c95}(t)$ of 100 consecutive events contained in a sliding window that is moved by one event each time are estimated. As shown in Figure 8c, the $m_{c95}(t)$ values quickly drop

from ~1.5 in the first 50 s, to around 0.2 after 200 s.

Next, we correct for the changing $m_c$ values and hence incompleteness in the catalogue at early times after the mainshock. We weight each aftershock based on the local $m_c$ using a weighting function $w(i) = 10^{[(m_c(i) - m_{c0}) \times b]}$, where $m_c(i)$ is the $m_c$ value for each event $i$, $b$ is exponent for the G-R relationship, $m_{c0}$ is the minimum $m_c$ value used in the analysis, equal to the long-times value of $m_c$. We use $b = 0.81$ and $m_{c0} = 0.2$ from the results shown in Figure 8. That is, $w(i) = 1$ if $m_c(i) = 0.2$, but $w(i) > 1$ if $m_c(i) > 0.2$. Events with magnitude $m_c < m_c(i)$ are not used in the analysis. By doing so, we assume that the aftershock size distribution follows the G-R relation immediately after the mainshock and does not change over time [*Kagan*, 2004]. Since foreshocks occur before the mainshock and are relatively free from the coda masking of previous events, we did not apply this correction for the foreshock seismicity rate.

**4.3 Seismicity rate before and after the mainshock**

Finally, we compute the seismicity rate for the 82 sequences after correcting for the changing $m_c$ value. Previous studies often use a fixed time window to compute seismicity rate based on the aftershock occurrence time [e.g., *Kagan*, 2004]. If the data is non-uniform, especially at times immediately before and after the mainshock, this may result in a time window with no data points, causing a gap in the obtained seismicity rate. So we use a moving data window [e.g., *Ziv et al.*, 2003; *Felzer and Brodsky*, 2006], instead of a moving time window to avoid this problem. Each data point corresponds to the time for an event relative to the mainshock. We use a fixed window of 5 data points, and the window slides by

one data point each time. Using different window sizes produces similar results. Seismicity rate computed from larger-size window is smoother, but the rate is less 'instantaneous' as compared with that from smaller-size window.

The results for both foreshocks and aftershocks are shown in Figure 9. To measure the change in seismicity rate, we fit the early and later aftershock rates separately using the Omoris law ($r(t) \sim 1/t^p$). The $p$ values obtained by a least-squares fitting are 0.58±0.08 between 20 and 900 s for the handpicked aftershocks, and 0.92±0.04 between 900 s and 3 days for aftershocks listed in the catalogue. The error is the 95% confidence interval based on 1000 bootstraps of the aftershock time.

In comparison, the seismicity rate for the foreshock sequences follows an inverse Omori's law with a $p$ value of 0.73±0.07 from several tens of days up to several hundreds of seconds before the mainshock. The seismicity rates for both foreshocks and aftershocks appear to merge with the background rates around several hundred days. However, they differ by 1 to 2 orders of magnitude around the mainshock occurrence time. This implies that the increase in foreshocks is lower than the decrease in aftershocks. Finally, the foreshock rate at 6-200 s before the mainshock is scattered due to the small amount of data, but the obtained $p$ value of 0.36±0.45 is lower than the foreshock increase rate at larger times. We did not include foreshocks that are within 6 s of the mainshock occurrence time (the peak amplitude for the mainshock in this study) to avoid masking by the *P*-wave arrival of the mainshock.

### 4.4 Statistical significance of a low early aftershock rate

The deficiency in seismicity immediately after the mainshock is statistically significant.

Assuming that an aftershock sequence is a Poisson process that follows the Omori's law, we can directly compare the number of aftershocks observed at early times with the expected number of events using the Omori's law with the $p$ value from later times. The maximum magnitude of completeness at short times ($20 \leq t \leq 100$ s) is 1.5. Extrapolating the long-term Omori's law ± uncertainties to this time range for events with $m \geq 1.5$, we expect to have [32 – 45] events. The observed number in this time and magnitude interval is 16. The probability of having no more than 16 events for a Poisson distribution with an expected number of [32 – 45] is [$5 \times 10^{-7}$ – 0.001]. Thus, the aftershock rate at short times $20 \leq t \leq 100$ s is significantly less than expected from the long-term aftershock rate at the 99.9% confidence level.

**4.5 Dependence of the *p* values on different parameters**

The result shown in Figure 9 is based on $m_{c0} = 0.2$ for immediate foreshocks and early aftershocks, and $m_{c0} = 0.7$ for long-term foreshocks and aftershocks. We also use the pre-event noise level + 0.3 magnitude shift as a measure of $m_c$ for each handpicked event. We systematically vary the choosing parameters to test their influences on the $p$ values. As shown in Figure 10, the $p$ values do not depend strongly on $m_{c0}$ ranging from −1 to 2. But there is slight increase of $p$ values for early aftershocks if we increase the magnitude shift from 0 to 1. At a magnitude shift of 1, there is no significant difference in the $p$ value for short and large times. However, a value of 1 means that we can only detect an event if its amplitude is about 10 times the pre-event noise level, which is well above the ability we can detect an event. Based on the hand-picked experience, a value of 0.3 (close to a signal-to-noise ratio of 2) is close to the true identification ability (i.e., magnitude of completeness) at the time of each

handpicked event.

The weighting procedure as described in Section 4.2 is employed to correct the changing completeness levels during the coda of the mainshock and large aftershocks. However, it does not consider the fact that many aftershocks may occur close in time. When the seismicity rate is high immediately after the mainshock, this will result in mixed phase arrivals that are difficult to be associated with individual event. Thus some events may not be clearly identified, causing a lower $p$ value in the early aftershock period than those at larger times. In addition, misidentification of events, especially for the smaller events, may cause the proportion of small/large aftershocks (i.e., the $b$ value of the magnitude distribution) to be smaller at early times compared to that at later times. Alternatively, the change in $p$ and $b$ values may be a real effect. For example, *Ziv et al.* [2003] have shown from relocated catalogue of microearthquakes in northern California that the $b$ value within $10^4$ s of a previous earthquake is significantly lower than that of the long-term value. *Shcherbakov et al.* [2006] found that the $b$ value increased from 0.60±0.01 after 0.1 day to 0.89±0.01 after 365 days in the aftershock zone of the 2004 Parkfield earthquake. However, these studies use aftershocks listed in the catalogue. So the effect of catalogue incompleteness on the $p$ and $b$ values cannot be ruled out.

To check if mixing of phase arrivals cause a significant number of missing aftershocks in our study, we evaluate the dependence of $p$ value on the aftershock productivity. If mixing of phase arrivals is mainly responsible for the lower $p$ value at early times, we should have higher $p$ values for the less productive sequences. So we order the 82 sequences according to the number of aftershocks with $m \geq 0$ observed in 100 days, and divide them into two groups

such that each group has roughly the same number of aftershocks. The first group has 12 sequences, and is considered as the productive group, as compared with the second group, which has 70 sequences. Figure 11 shows that early aftershock decay rates are similar for both groups, despite a factor of 5-6 differences in aftershock productivity. This indicates that we do not miss a significant fraction of aftershocks due to mixed phase arrivals. We also check the dependence of $p$ values with the mainshock magnitude by separating the 82 sequences into four magnitude groups with 0.5 unit interval based on the mainshock magnitude (Figure 11b, c). We did not find a strong dependence of $p$ values for sequences with the mainshock magnitude $3 \leq m \leq 5$.

We note that it is possible that for aftershock sequences with larger mainshock magnitude (e.g., $m \geq 6$), a significant fraction of small events is missing due to mixed phase arrivals, and mainshock coda masking. For example, *Kagan* [2004] have shown that the number of small ($m \leq 3$) aftershocks that were missing in the time interval of 0-128 days exceeds those that were listed in the catalogue for the 1992 Landers earthquake. *Peng et al.* [2006] found that a significant fraction of events were missing in the Northern California Seismic Network catalogue in the first hour after the 2004 M6 Parkfield earthquake. However, we are confident from the above analysis that to the first order, mixed phase arrivals does not cause a significant change in the number of the aftershocks determined in this study.

**4.6 Direct estimation of the level of aftershock activity**

Results shown in previous sections are based on events listed in the JMA catalogue and identified by our handpicking procedure. If we assume that energy radiated at 30 Hz is

indicative of the level of seismic activity, the seismicity rate immediately before and after the mainshock can be directly obtained from the envelope functions without picking individual event. The envelope stack is obtained by summing the square of the envelope function for all 82 sequences, and taking the square root and logarithm (based 10). Since each individual envelope has different noise level before the mainshock, directly stacking the envelope functions would bias the result toward those that have higher background noise levels. Thus, we shift each envelope using the average values from 180 to 150 s before the mainshock (when the foreshock activity is relatively low) to achieve a similar noise level (near zero). The choice of offset is somewhat arbitrary, but helps to separate features that are near the noise level (near zero) and those well above the noise level.

The resulting stacked envelope is shown in Figure 12a in linear time scale. The coda from the mainshocks disappears into the signal from the aftershocks at ~30 s, and the rest of the curve represents the level of the aftershock activity. Figure 12b shows the stacked envelope functions in logarithmic time scale. We smooth the envelope by convolving the log time with a Gaussian kernel of width 0.08 [*Helmstetter and Shaw*, 2006]. The best-fitting $p$ value for envelopes between 30 and 900 s after the mainshock is 0.69, close to that estimated from the handpicked catalogue. Measuring uncertainty on the obtained $p$ value is difficult, because it depends on how the curve is been smoothed.

Figure 12b also shows that a burst with the largest foreshocks is visible between 150-120 s before the mainshock. This is consistent with a cluster of handpicked events shown in Figure 7b. It is clear that the foreshock activity does not fit the inverse Omori's law in the last 200 s before the mainshock. Also there is a relative quiescence in the last few tens of seconds,

which is evident in the lack of handpicked events in that time period (Figure 6b).

## 5. Interpretation

Figure 13 compare the *p* values obtained in this study as a function of time before and after the mainshock. The early aftershock decay rate is smaller than the late aftershock decay rate. The foreshock increase rate is smaller than the aftershock decay rate, and the immediate foreshock rate is smaller than the long-term foreshock rate. Below we will discuss possible interpretations that can explain observations for aftershocks and foreshocks separately.

### 5.1 Possible interpretations for aftershock decay rate

The decay of the number of aftershocks with time has been observed for more than a century. However, the underlying physics for such time-dependent phenomena remains unclear. Aftershock triggering is more commonly explained by the static stress change induced by the mainshock [e.g., *Stein*, 1999], but dynamic stress changes associated by the mainshock have also been invoked [*Gomberg et al.*, 1997; *Brodsky et al.*, 2003; *Parsons*, 2005]. The decay of the number of aftershocks with time can also be explained by postseismic stress relaxation following the mainshock, which can result from fluid flow [*Nur and Booker*, 1972], viscous relaxation [*Mikumo and Miyatake*, 1979] or aseismic slip [*Benioff*, 1951; *Schaff et al.,* 1998; *Peng et al.*, 2005; *Zoller et al.*, 2005]. Many mechanisms have been proposed to explain earthquake triggering by stress changes, such as stress corrosion [*Das and Scholz*, 1981; *Yamashita and Knopoff*, 1987; *Gomberg*, 2001], rate-and-state friction [*Dieterich*, 1994], and damage rheology [*Ben-Zion and Lyakhovsky*, 2006].

Among them, we focus on the rate-and-state (RS) model [*Dieterich*, 1994] that has been widely applied to explain the time-dependence of aftershock activity. This model assumes that populations of faults around the mainshock rupture obey the laboratory-derived RS friction law [*Dieterich*, 1979]. If the loading rate is increased uniformly due to a mainshock, the change in seismicity can be approximated by the Omori's law with $p = 1$ for intermediate times after the mainshock. At very short times, i.e., times less than a characteristic time $c = t_a e^{-\tau / A\sigma}$ (where $t_a$ is aftershock duration, $A$ is a parameter of the rate-and-state friction law, $\tau$ is the coseismic stress change, and $\sigma$ is the normal stress), the seismicity rate is constant. The seismicity rate returns to the background seismicity rate at very long times.

Our observation of a small $p$ value immediately after the mainshock is consistent with the RS model. However, we did not find a clear gap of activity (or flatting of seismicity rate) since 10 s after the mainshock. This indicates that the $c$ value, if exists, is likely to be very small (< 10 s) in our data. Recent studies have shown the existence of small, but non-zero $c$ values (on the order of a few minutes) in the early aftershock decay rate for several large earthquakes in Japan and California [*Vidale et al.*, 2003; *Enescu et al.*, 2006; *Peng et al.*, 2006]. The difference might be due to the mainshock magnitude, employed techniques, or systematic bias by missing early aftershocks.

The epidemic-type aftershock sequence (ETAS) model [*Kagan and Knopoff*, 1981; *Ogata*, 1988; *Helmstetter and Sornette*, 2002] can also explain our observed foreshock and aftershock rates. This model assumes that each earthquake can trigger other earthquakes according to the modified Omori law with an exponent $p$ larger than 1. However, because of cascades of

earthquake triggering, the observed Omori exponent in this model is smaller than 1 at short times, and increases slowly with time [*Helmstetter and Sornette*, 2002; *Helmstetter et al.*, 2003], as observed in our data.

### 5.2 Mapping aftershock rate into spatial stress distribution

Since the coseismic stress change $\tau$ is likely to be different at each aftershock nucleation point, this will result in different characteristic time $c$ overlapping with each other. Thus, the observed aftershock rate is a superposition of those from different stress values, and the observed rate may be used to infer stress distribution after the mainshock.

There are two possible ways to map temporal changes of aftershock rate into spatial stress distribution. *Dieterich* [1994] showed that, if the mainshock is modeled as a dislocation, aftershock rate within a finite time interval and region decays with the $p$ value of ~0.8, due to a non-uniform stress change around the mainshock. Because the stress change decreases with the distance $r$ from the crack tip, this model also gives an apparent Omori exponent that decreases with $r$ [*Dieterich*, 1994].

In this study, we compute seismicity rate using all events within one-rupture length of the mainshock. The observed $p$ value for long-term aftershocks is 0.92±0.04. This value is close to the aftershock decay rate of $p \sim 0.8$ predicted by the RS model for a finite region surrounding a shear crack [*Dieterich*, 1994]. However, this model does not explain our observation of a smaller $p$ value at short times than that for larger times. At very short times in the RS model, the large stress drop resulting from a singularity at the crack tip control the seismicity. This gives a $p$ value that increases progressively toward $p = 1$ as times decreases

to the mainshock occurrence. In contrast, we find $p$ value of ~0.6 immediately after the mainshock.

*Dieterich* [1994] assumed that stress drop is uniform across the mainshock rupture area. This model would predict no aftershocks on or very close to the rupture surface. Some studies have shown an anti-correlation between the mainshock slip area and the aftershock distribution [e.g., *Mendoza and Hartzell*, 1998; *Schaff et al.*, 2002]. However, aftershocks do occur very close to the rupture surface of the mainshock, although the fraction of events occurring on and off the mainshock slip plane remains unclear [*Liu et al.*, 2003]. This observation suggests that the coseismic stress change on the mainshock fault plane is heterogeneous. The heterogeneity may be caused by slip fluctuations [*Herrero and Bernard*, 1994], or to the rugosity of the fault [*Dieterich*, 2005]. Additional evidences for a heterogeneous stress field come from both mainshock slip inversion [e.g., *Wald and Heaton*, 1994] and a high diversity of aftershock focal mechanisms [e.g., *Michael et al.*, 1990; *Hardebeck et al.*, 1998].

*Helmstetter and Shaw* [2006] and *Marsan* [2006] proposed a method to estimate distributions of stress heterogeneity from the aftershock rate based on the RS model [*Dieterich*, 1994]. Instead of mapping changes in seismicity onto time-dependent stress changes [*Dieterich et al.*, 2000], they mapped subtle but significant deviations from the pure Omori's law onto measures of stress heterogeneity on the mainshock rupture area. *Helmstetter and Shaw* [2006] showed that the $p$ value increases toward 1 with increasing stress heterogeneity. Furthermore, using the scale invariant "$k^2$" slip model [*Herrero and Bernard*, 1994], they produced an aftershock rate that is close to the Omori's law with $p \leq 1$. In this

stress heterogeneity model, the $p$ value increases slowly with time, which is consistent with our observation.

We have applied this technique to our catalogue. We fit the aftershock rate by the RS model, assuming that the Coulomb stress change, in the region where we select aftershocks, has spatial fluctuations that can be modeled by a Gaussian distribution. This stress distribution can be obtained, for instance, by the kinematic "$k^2$" slip model [*Herrero and Bernard*, 1994]. We fit the aftershock rate $R(t)$ in the time range 10 s – 100 days by the function [*Dieterich*, 1994; *Helmstetter and Shaw*, 2006]

$$R(t) = \int_{-\infty}^{\infty} \left[ \frac{R_r}{(e^{-\tau / A\sigma} - 1)e^{-t/t_a} + 1} \right] \left[ \frac{1}{\tau^* \sqrt{2\pi}} \right] e^{\frac{-(\tau - \tau_0)^2}{2(\tau^*)^2}} d\tau \,, \qquad (2)$$

where $R_r$ is the reference seismicity rate, $\tau_0$ is the average stress change, and $\tau^*$ is the standard deviation of the stress change. There are 3 unknown parameters in this function, the normalized average stress change $\tau_0 / A\sigma$, the standard deviation $\tau^* / A\sigma$, and the aftershock duration $t_a$. The reference rate $R_r = 2\text{x}10^{-7}$ events/s with $m \geq 1$ was estimated from the average seismicity rate at large times before the mainshock (i.e., $\geq 10^7$ s). We use a least-squares minimization to invert for $\tau_0 / A\sigma$, $\tau^* / A\sigma$, and $t_a$ from the observed aftershock rate. The problem is poorly constrained for 3-parameter inversion, thus we assume that the average stress change is 0. This is justified because we select aftershocks over an area larger than the mainshock rupture length. The large stress increase around the rupture area roughly compensates for the average stress decrease on the rupture area. The stress change averaged over an infinite area is equal to zero, while its absolute value is equal to the stress drop if we average over the rupture area. The inversion gives $\tau^* / A\sigma = 10.6$ and $t_a = 0.88$ yr (Figure 14).

If the average stress change is –1.5, we obtain $\tau^* / A\sigma = 11.2$ and $t_a = 1.01$ yr.

There is a large uncertainty on the value of $A\sigma$ in the crust. Assuming $A = 0.01$, as measured in laboratory friction experiments [*Dieterich*, 1994], and $\sigma = 100$ MPa (corresponding to the lithostatic pressure at a depth of about 5 km), this gives $A\sigma = 1$ MPa. Using a typical stress drop of 3 MPa, *Dieterich* [1994] found $A\sigma = 0.15$ MPa, from the relation between aftershock duration and mainshock recurrence time. *Cochran et al.* [2004] used the RS model to explain tidal triggering of earthquakes, and obtained a preferred value of $A\sigma = 0.064$ MPa, and an acceptable range $0.048 < A\sigma < 0.11$ MPa. Moreover, there are probably large spatial fluctuations of $A\sigma$ in the crust. Heterogeneity of $A\sigma$ also modifies the time decay of aftershocks [*Helmstetter and Shaw*, 2006], and can bias the value of $\tau^*$ obtained by assuming that $A\sigma$ is constant in space and time. We can thus conclude that the RS model, with stress heterogeneity, can explain our observations (Omori exponent smaller than 1, and increasing slowly with time). However, it is difficult, from the observed seismicity rate $R(t)$ alone, to characterize the stress heterogeneity, and to distinguish different sources of heterogeneity (Coulomb coseismic stress change $\tau$, parameter A of the friction law, and normal stress $\sigma$).

**5.3 Possible interpretations for foreshock increase rate**

Our results indicate that the foreshocks follow the inverse Omori's law, but the foreshock increase rate is smaller than the aftershock decay rate, and there appears to be a peak of foreshock activity ~100 s before the mainshock. There are two possible models to explain the relationship between the foreshocks and mainshocks. The first is that foreshocks change the

stress distribution and the mainshock. The second is that foreshocks are caused by a change of stress field related to a mainshock.

The first model is compatible with the ETAS model, and models of earthquake triggering such as the RS model [*Dieterich*, 1995; *Ziv*, 2003], in which cascade of events trigger future events with the same physical mechanism [*Jones et al.*, 1995; *Kilb and Gomberg*, 1999; *Felzer et al.*, 2004]. Using this model, the rate of foreshocks is predicted to increase following the inverse Omori's law [*Helmstetter et al.*, 2003; *Helmstetter and Sornette*, 2003]. This is consistent with our observation of a power law increase of foreshock occurrences.

The fact that Omori exponent $p$ is smaller for foreshocks than for aftershocks is also in agreement with the predictions of the ETAS model [*Helmstetter et al.*, 2003]. *Ziv* [2003] used numerical simulations of the RS model, and found that the Omori exponent $p$ is slightly smaller for foreshocks than for aftershocks. In his model, exponents for both fore- and aftershocks are smaller or equal to 1, and decrease as the distance from the mainshock decreases. An observation that is consistent with this prediction was made from time distribution of foreshocks of several hundred mainshocks with $m \geq 5.0$ listed in the JMA catalogue from 1977 to 1997 [*Maeda*, 1999].

The foreshock increase rate in our data may also be influenced by our selection rule for the mainshock. We did not include an earthquake that was preceded by a larger event as a potential mainshock. In comparison, an earthquake that was followed by a larger event is considered as a potential mainshock. Such rule may lower the average acceleration of the seismicity before the mainshock, and hence lower the Omori exponent for foreshocks.

We also observed that there is a slight dependence of foreshock rate with the $m_c$ value: the

rate of larger events is higher than that of smaller events (Figure 10). In addition, there is a lack of small events in the last 20 s before the mainshock. These results are expected by the triggering model such as ETAS: because a large foreshock is more likely to trigger the mainshock than a smaller one, the magnitude distribution deviates from the average distribution [*Michael and Jones*, 1998; *Helmstetter et al.*, 2003; *Helmstetter and Sornette*, 2003]. If the long-term magnitude distribution obeys the G-R law $P(m) \sim 10^{-bm}$, where $P(m)$ is the number of events with magnitude $\geq m$, and aftershock productivity scales as $10^{am}$ with the mainshock magnitude $m$, the magnitude distribution of foreshocks at short times before the mainshock is $\sim 10^{-(b-a)m}$. This results in a small apparent $b$ value.

The peak of foreshock activity at ~100 s before the mainshock may be due to statistical fluctuations. The Omori's law decay is generally observed for each individual aftershock sequence, while the inverse Omori's law is observed only on stacked foreshock sequences, due to larger fluctuations in the foreshock rate than in the aftershock rate. In addition, foreshocks usually occur in clusters, which may explain the peak observed in the data. We have generated synthetic ETAS catalogues, which reproduce qualitatively our results: increase of $p$ value with time for foreshocks and aftershocks, lower $p$ value for foreshocks than for aftershocks, and large fluctuations of the foreshock rate.

In the second model, foreshocks and mainshock nucleation are considered as a consequence of non-seismic stress change associated with the mainshock [e.g., *Dodge and Beroza*, 1996; *Olson and Allen*, 2005]. Possible candidates for the non-seismic stress changes are episodic aseismic slip [*Linde et al.*, 1996; *Nadeau and McEvilly*, 2004; *McGuire*, 2003; *McGuire et al.*, 2005], pore fluid pressure fluctuations [e.g., *Ake et al.*, 2005], dike injection

[e.g, *Smith et al.*, 2004], and sometimes a combination of these candidates [*Hainzl and Ogata*, 2005].

*Vidale and Shearer* [2006] systematically investigated 71 earthquake bursts in southern California, and found evidence many bursts of activities are driven by underlying geophysical disturbance such as episodic aseismic slip, or pore fluid pressure fluctuations, rather than simple elastic stress triggering. Based on stacked global earthquake sequences, *Jones and Molnar* [1979] found that foreshock activity rises a few days before the mainshock and peaks 1-2 hours before the mainshock. *Chen et al.* [1999] showed that foreshocks are separated by a few hours of quiescence from several major earthquakes in China. *Zanzerkia et al.* [2003] identified two clusters of foreshock sequences, one between 20 to 13 hours and the other starting 8 hours before the 1999 Hector Mine earthquake. *McGuire et al.* [2005] found higher rates of foreshocks and lower rates of aftershocks on the oceanic East Pacific Rise transform faults. They inferred that slow slip events, which accommodate most of the aseismic plate motion on those faults, trigger the earthquake sequences. A concentration of foreshock activity in the last 100-1000 s before the mainshock observed on these oceanic transform faults [*McGuire*, 2003] is similar to our observation of a peak in foreshock activity at ~100 s before the mainshock. It is possible that concentration of foreshock activity may differ for individual sequence, or is related to the mainshock magnitude. Our study involves waveform recording of the last 200 s before the mainshock, so the possibility of intense foreshock activity at earlier times cannot be ruled out.

## 6. Conclusions

We have analyzed foreshock and aftershock rates of 82 shallow earthquake sequences (depth ≤ 30 km) with mainshock magnitude $3 \leq m \leq 5$ in Japan using waveforms recorded by the Hi-net borehole array. By scrutinizing high-frequency signals, we have detected 5 times as many aftershocks in the first 200 s as listed in the JMA catalogue. The difference between the aftershocks listed in the JMA catalogue and the additional events identified by our procedure indicates that seismic activity immediately before and after the mainshock can be obtained from high-quality continuous waveform data.

After correcting for the changing completeness level immediately after the mainshock, we find that early aftershocks decay slower than the late aftershocks. Similarly, the seismicity rate for the foreshock sequences follows an inverse Omori's law with a $p$ value of ~.7 from several hundred days up to near the mainshock occurrence time. The seismicity rate in the last 200 s before the mainshock appears steady instead of increasing with time.

These observations can be explained by the ETAS model, and the rate-and-state model [*Dieterich*, 1994] for a heterogeneous stress change along the fault plane [*Dieterich,* 2005; *Marsan*, 2006; *Helmstetter and Shaw*, 2006]. Alternatively, seismicity around the mainshock may be caused by non-seismic stress changes around the source region, due, for example, to episodic aseismic slip or pore fluid pressure fluctuations.

## Acknowledgments

We thank the National Research Institute for Earth Science and Disaster Prevention in Japan for making the Hi-net data available. Yehuda Ben-Zion, Emily Brodsky, Jim Dieterich, Karen Felzer, Heidi Houston, Debi Kilb, Bruce Shaw, and Yan Kagan generously provided

commentary. The analysis is done using the Seismic Analysis Code [*Goldstein et al.*, 2003] and GMT [*Wessel and Smith*, 1998]. This work is supported by UC Lawrence Livermore National Laboratory (US. DOE) 04-GS-026, and Southern California Earthquake Center (SCEC). SCEC is funded by NSF Cooperative Agreement EAR-0106924 and USGS Cooperative Agreement 02HQAG0008. The SCEC contribution number for this paper is 1029.

**References**

Abercrombie, R. E. and J. Mori (1996), Occurrence patterns of foreshocks to large earthquakes in the western United States, *Nature*, *381*, 303–307.

Ake, J., K. Mahrer, D. O'Connell, and L. Block (2005), Deep-injection and closely monitored induced seismicity at Paradox Valley, Colorado, *Bull. Seism. Soc. Am.*, *95*, 664–683.

Aki, K., (1969), Analysis of seismic coda of local earthquakes as scattered waves, *J. Geophys. Res.*, *74*, 615–631.

Benioff, H. (1951), Earthquakes and rock creep. Part I: Creep characteristics of rocks and the origin of aftershocks, *Bull. Seismol. Soc. Am.*, *41*, 31–62.

Ben-Zion, Y., and Y. Lyakhovsky (2006), Analysis of aftershocks in a lithospheric model with seismogenic zone governed by damage rheology, *Geophys. J. Int., 165*, doi: 10.1111/j.1365-246X.2006.02878.x.

Brodsky, E. E., E. Roeloffs, D. Woodcock, I. Gall, and M. Manga (2003), A mechanism for sustained groundwater pressure changes induced by distant earthquakes, *J. Geophys. Res.*, *108*(B8), 2390, doi: 10.1029/2002JB002321.

Chen, Y., J. Liu, and H. Ge (1999), Pattern characteristics of foreshock sequences, *Pure Appl. Geophys.*, *155*, 395–408.

Cochran, E. S., J. E. Vidale, S. Tanaka (2004), Earth tides can trigger shallow thrust fault earthquakes, *Science*, 306, 1164–1166.

Das, S., and C. Scholz (1981), Off-fault aftershock clusters caused by shear stress increase?, *Bull. Seismol. Soc. Am.*, *71*, 1669–1675.

Dieterich, J. H. (1979), Modeling of rock friction: 1. Experimental results and constitutive equations, *J. Geophys. Res.*, *84*, 2161–2168.

Dieterich, J. H. (1994), A constitutive law for rate of earthquake production and its application to earthquake clustering, *J. Geophys. Res.*, 99, 2601–2618.

Dieterich, J. H. (1995), Earthquake simulation with time-dependent nucleation and long-range interactions, *Nonlin. Processes Geophys.*, 2, 109–120.

Dieterich, J. H. (2005), Role of stress relaxation in slip of geometrically complex faults, *Eos Trans. AGU*, *86*(52), Fall Meet. Suppl., Abstract NG31A-04.

Dieterich, J. H., V. Cayol, and P. Okubo (2000), The use of earthquake rate as a stress meter at Kilauea volcano, *Nature*, *408*, 457–460.

Dodge, D. A., G. C. Beroza, and W. L. Ellsworth (1996), Detailed observations of California foreshock sequences: implications for the earthquake initiation process, *J. Geophys. Res.*, *101*, 22,371–22,392.

Enescu, B., J. Mori and M. Miyazawa (2006), Quantifying early aftershock activity of the 2004 Mid Niigata Prefecture Earthquake (Mw6.6), *J. Geophys. Res.*, submitted.

Eshelby, J.D. 1957. The determination of the elastic field of an ellipsoidal inclusion and

related problems. *Proc R. Soc. Lond. A*, *241*, 376–396.

Felzer, K. R. and E. E. Brodsky (2006), Decay of aftershock density with distance indicates triggering by dynamic stress, *Nature*, 441, 735–738.

Felzer, K. R., R. E. Abercrombie, and G. Ekstrom (2004), A common origin for aftershocks, foreshocks, and multiplets, *Bull. Seismol. Soc. Am.*, *94*, 88–98.

Geller, R. J., D. D. Jackson, Y. Y. Kagan, and F. Mulargia (1997), Earthquakes cannot be predicted, *Science*, *275*, 1616.

Gerstenberger, M. C., S. Wiemer, L. M. Jones, and P. A. Reasenberg (2005), Real-time forecasts of tomorrow's earthquakes in California, *Nature*, *435*, 328–331, doi:10.1038/nature03622.

Goldstein, P., D. Dodge, M. Firpo, and L. Minner (2003), SAC2000: Signal processing and analysis tools for seismologists and engineers, In The IASPEI International Handbook of Earthquake and Engineering Seismology, Part B, Chapter 85.5, ed. W.H.K. Lee, H. Kanamori, P. C. Jennings, and C. Kisslinger, Academic Press, London.

Gomberg, J. (2001), The failure of earthquake failure models, *J. Geophys. Res.*, *106*, 16,253–16,264.

Gomberg, J., M. L. Blanpied, N. M. Beeler, and P. Bodin (1997), Transient triggering of near and distant earthquakes, *Bull. Seismol. Soc. Am.*, *87*, 294–309.

Gutenberg, R., and C. F. Richter (1944), Frequency of earthquakes in California, *Bull. Seismol. Soc. Am.*, *34*, 185–188.

Hainzl, S., and Y. Ogata (2005), Detecting fluid signals in seismicity data through statistical earthquake modeling, *J. Geophys. Res.*, *110*, B05S07, doi:10.1029/2004JB003247.

Hardebeck, J. L., J. J. Nazareth, and E. Hauksson (1998). The static stress change triggering model: constraints from two southern California aftershock sequences, *J. Geophys. Res.*, *103*, 24,427–24,437.

Helmstetter, A., and D. Sornette (2002), Subcritical and supercritical regimes in epidemic models of earthquake aftershocks, *J. Geophys. Res.*, *107*(B10), 2237, doi:10.1029/2001JB001580.

Helmstetter, A., and D. Sornette (2003), Foreshocks explained by cascades of triggered seismicity, *J. Geophys. Res.*, *108*, 2457, 10.1029/2003JB002409.

Helmstetter, A., and B. E. Shaw (2006), Relation between stress heterogeneity and aftershock rate in the rate-and-state model, J. Geophys. Res., 111, B07304, doi:10.1029/2005JB004077.Helmstetter, A., D. Sornette, and J.-R. Grasso (2003), Mainshocks are aftershocks of conditional foreshocks: How do foreshock statistical properties emerge from aftershock laws, *J. Geophys. Res.*, *108*, 2046, doi:10.1029/2002JB001991.

Helmstetter, A., Y. Kagan, and D. Jackson, (2005), Importance of small earthquakes for stress transfers and earthquake triggering, *J. Geophys. Res.*, *110*, B05S08, 10.1029/2004JB003286.

Helmstetter, A., Y. Kagan and D. D. Jackson (2006), Comparison of short-term and long-term earthquake forecast models for southern California, *Bull. Seismol. Soc. Am*., *76*(1), 90-106.

Herrero, A., and P. Bernard (1994), A kinematic self-similar rupture process for earthquakes, *Bull. Seismol. Soc. Am*., *84*, 1216–1228.

Jones, L. M., and P. Molnar (1979), Some characteristics of foreshocks and their possible relationship to earthquake prediction and premonitory slip on fault, *J. Geophy. Res.*, *84*, 3596–3608.

Jones, L. M., R. Console, F. Di Luccio, and M. Murru (1995), Are foreshocks mainshocks whose aftershocks happen to be big? Evidence from California and Italy (abstract), *EOS Trans. AGU, 76(46), Fall Meet. Suppl.*, F388.

Kagan, Y. Y. (1991), Seismic moment distribution, *Geophys. J. Int.*, *106*, 123–136.

Kagan Y. Y. (2003), Accuracy of modern global earthquake catalogues, *Phys. Earth Planet. Inter., 135*(2-3), 173–209.

Kagan, Y. Y. (2004), Short-term properties of earthquake catalogues and models of earthquake source, *Bull. Seismol. Soc. Am.*, *94*(4), 1207–1228.

Kagan, Y. Y., and L. Knopoff (1981), Stochastic synthesis of earthquake catalogues, *J. Geophys. Res.*, *86*, 2853–2862.

Kagan, Y. Y., and H. Houston, (2005), Relation between mainshock rupture process and Omori's law for aftershock moment release rate, *Geophys. J. Int.*, *163*(3), 1039-1048.

Kilb D., and J. Gomberg (1999), The initial subevent of the 1994 Northridge, California, Earthquake: Is earthquake size predictable?, *J. Seismol.*, 3, 409–420.

Kilb, D., V. G. Martynov, and F. L. Vernon (2004), Spatial/Temporal interdependence of aftershocks following the 10/31/2001 M5.1 Anza Earthquake, *Eos Trans. AGU,* 85(47), Fall Meet. Suppl., Abstract S54A-02.

Kisslinger, C. (1996), Aftershocks and fault-zone properties, in *Advances in Geophysics*, vol. 38, pp. 1–36, Academic, San Diego, Calif.

Kisslinger, C., and L. M. Jones (1991), Properties of aftershock sequences in southern California, *J. Geophys. Res.*, *96*, 11,947–11,958.

Linde, A. T., M. T. Gladwin, M. J. S. Johnston, R. L. Gwyther, and R. G. Bilham (1996), A slow earthquake sequence on the San Andreas fault, *Nature*, *383,* 65–68.

Liu, J, K. Sieh, E. Hauksson (2003), A structural interpretation of the aftershock "cloud" of the 1992 Mw 7.3 Landers earthquake, *Bull. Seismol. Soc. Am.*, *93*, 1333–1344.

Lolli, B. and P. Gasperini (2006), Comparing different models of aftershock rate decay: the role of catalogue incompleteness in the first times after mainshock, *Tectonophysics*, in press.

Maeda, K. (1999), Time distribution of immediate foreshocks obtained by a stacking method, *Pure Appl. Geophy.*, *155*, 381–394.

Marsan D. (2006), Can coseismic stress variability suppress seismicity shadows? Insights from a rate-and-state friction model, *J. Geophys. Res.*, 111, B06305, 10.1029/2005JB004060.

McGuire, J. J., (2003), Immediate foreshock sequences of oceanic transform earthquakes on the East Pacific Rise, *Bull. Seismol. Soc. Am.*, *93*(2), 948–952.

McGuire, J. J., M. S. Boettcher, and T. H. Jordan (2005), Foreshock sequences and short-term earthquake predictability on East Pacific Rise transform faults, *Nature*, *434*, 457–461, doi: 10.1038/nature03377.

Mendoza, C., and S. H. Hartzell (1988), Aftershock patterns and mainshock faulting, *Bull. Seismol. Soc. Am., 78*, 1438–1449.

Michael, A. J. and L. M. Jones (1998), Seismicity alert probabilities at Parkfield, California,

revisited, *Bull. Seis. Soc. Am.*, *88*, 117–130.

Michael, A. J., W. L. Ellsworth, and D. Oppenheimer (1990). Co-seismic stress changes induced by the 1989 Loma Prieta, California earthquake, *Geophys. Res. Lett.*, *17*, 1441–1444.

Mikumo, T., and T. Miyatake (1979), Earthquake sequences on a frictional fault model with non-uniform strengths and relaxation times, *Geophys. J. R. Astron. Soc.*, *59*, 497–522.

Mogi, K. (1962), Study of the elastic shocks caused by the fracture of heterogeneous materials and its relation to earthquake phenomena, *Bull. Earthq. Res. Inst., Univ. Tokyo*, *40*, 125–173.

Mori, J. J., and Abercrombie, R. E. (1997), Depth dependence of earthquake frequency-magnitude distributions in California: implications for rupture initiation, *J. Geophys. Res., 102*, 1508115090.

Nadeau, R. M., and T. V. McEvilly (2004), Periodic pulsing of characteristic microearthquakes on the San Andreas Fault, *Science*, *303*(5655), 220–222.

Nanjo, K., H. Nagahama, and M. Satomura (1998), Rates of aftershock decay and the fractal structure of active fault systems, *Tectonophysics*, *287*, 173–186.

Narteau, C., P. Shebalin, and M. Holschneider (2002), Temporal limits of the power law aftershock decay rate, *J. Geophys. Res.*, *107*(B12), 2359, doi:10.1029/2002JB001868.

Nur A., and J. R. Booker (1972), Aftershocks caused by pore fluid flow? *Science*, *175*, 885–888.

Ogata, Y. (1988), Statistical models for earthquake occurrence and residual analysis for point processes, *J. Am. Stat. Assoc.*, *83*, 9–27.

Okada, Y., K. Kasahara, S. Hori, K. Obara, S. Sekiguchi, H. Fujiwara, and A. Yamamoto (2004), Recent progress of seismic observation networks in Japan -Hi-net, F-net, K-NET and KiK-net, *Earth Planet Space*, *56*, xv-xxviii.

Olson, E.L., and R.M. Allen (2005). The deterministic nature of earthquake rupture. *Nature*, 438, 212–215, doi:10.1038/nature04214.

Parsons, T. (2005), A hypothesis for delayed dynamic earthquake triggering, *Geophys. Res. Lett.*, *32*, L04302, doi:10.1029/2004GL021811.

Peng, Z., J. E. Vidale, C. Marone, and A. Rubin (2005), Systematic variations in moment with recurrence interval of repeating aftershocks, *Geophys. Res. Lett.*, *32*(15), L15301, doi: 10.1029/2005GL022626.

Peng, Z., J. E. Vidale, and H. Houston (2006), Anomalous early aftershock decay rate of the 2004 Mw6.0 Parkfield, California, earthquake, *Geophys. Res. Lett.*, in press, doi: 10.1029/2006GL026744.

Reasenberg P. A. (1999), Foreshock occurrence before large earthquakes, *J. Geophy. Res.*, *104*, 4755–4768.

Reasenberg, P. A., and L. M. Jones (1989), Earthquake hazard after a mainshock in California, *Science*, *243*, 1173–1176.

Reasenberg, P. A., and L. M. Jones (1994), Earthquake aftershocks: Update, *Science*, *265*, 1251–1252.

Sato, H., and M. Fehler (1998), Seismic Wave Propagation and Scattering in the Heterogeneous Earth, Springer-Verlag and American Institute of Physics Press.

Schaff, D. P., G. C. Beroza, and B. E. Shaw (1998), Postseismic response of repeating

aftershocks, *Geophys. Res. Lett.*, *25*, 4549–4552.

Schaff, D. P., G. H. R. Bokelmann, G. C. Beroza, F. Waldhauser, and W. L. Ellsworth (2002), High resolution image of Calaveras Fault seismicity, *J. Geophys. Res.*, *107*(B9), 2186, doi:10.1029/2001JB000633.

Shcherbakov, R., D. L. Turcotte, and J. B. Rundle (2004), A generalized Omori's law for earthquake aftershock decay, *Geophys. Res. Lett.*, *31*, L11613, doi:10.1029/2004GL019808.

Shcherbakov, R. and D. L. Turcotte (2006), Scaling Properties of the Parkfield Aftershock Sequence, *Bull. Seismol. Soc. Am.*, *96*(4B), S376–S384.

Smith, K. D., D. V. Seggern, G. Blewitt, L. Preston, J. G. Anderson, B. P. Wernicke, and J. L. Davis (2004), Evidence for Deep Magma Injection Beneath Lake Tahoe, Nevada-California, *Science*, *305*(5688), 1277–1280.

Stein, R. S. (1999), The role of stress transfer in earthquake occurrence, *Nature*, *402*, 605–609.

Utsu, T. (1966), A statistical significance test of the difference in b-value between two earthquake groups, *J. Phys. Earth*, 14, 37–40, 1966.

Utsu, T., Y. Ogata, and R. S. Matsu'ura (1995), The centenary of the Omori formula for a decay law of aftershock activity, *J. Phys. Earth*, *43*(1), 1–33.

Vidale, J. E., and P. M. Shearer (2006), A survey of 71 earthquake bursts across southern California: Exploring the role of pore fluid pressure fluctuations and aseismic slip as drivers, *J. Geophys. Res., 111,* B05312, doi:10.1029/2005JB004034.

Vidale, J. E., E. S. Cochran, H. Kanamori, and R. W. Clayton (2003), After the lightning and

before the thunder; non-Omori behavior of early aftershocks? *Eos Trans. AGU 84(46), Fall Meet. Suppl.*, Abstract S31A-08.

Wald, D. J., and T. H. Heaton (1994), Spatial and temporal distribution of slip for the 1992 Landers, California, earthquake, *Bull. Seismol. Soc. Am.*, *84*, 668–691.

Wiemer, S., and K. Katsumata (1999), Spatial variability of seismicity parameters in aftershock zones. *J. Geophys. Res.*, *104*, 13135–13151.

Wiemer, S., and M. Wyss (2000), Minimum magnitude of completeness in earthquake catalogues: examples from Alaska, the western United States, and Japan, *Bull. Seismol. Soc. Am.*, *90*, 859–869.

Woessner, J., and S. Wiemer (2005), Assessing the quality of earthquake catalogues: estimating the magnitude of completeness and its uncertainty, *Bull. Seismol. Soc. Am.*, 95, 684-698.

Working Group On California Earthquake Probabilities (2003), Earthquake probabilities in the San Francisco Bay region: 2002– 2031, *U.S. Geol. Surv. Open File Rep., 03-214*.

Yamashita ,T., and Knopoff, L. (1987), Models of aftershock occurrence, *Geophys. J. R. Astr. Soc.*, *91*, 13–26.

Zanzerkia, E. E., G. C. Beroza, and J. E. Vidale (2003), Waveform analysis of the 1999 Hector Mine, California, foreshock sequence, *Geophys. Res. Lett.*, *30*(8), 1429, doi:10.1029/2002GL016612.

Zoeller, G., S. Hainzl, M. Holschneider, and Y. Ben-Zion (2005), Aftershocks resulting from creeping sections in a heterogeneous fault, *Geophys. Res. Lett.*, *32*, L03308, doi:10.1029/2004GL021871.

Ziv, A (2003), Foreshocks, aftershocks, and remote triggering in quasi-static fault models, *J. Geophys. Res.*, *108*, 2498, doi:10.1029/2002JB002318.

Ziv, A., A. M. Rubin, and D. Kilb (2003), Spatiotemporal analyses of earthquake productivity and size distribution; observations and simulations, *Bull. Seismol. Soc. Am.*, *93*, 2069–2081.

**Figure captions**

Figure 1. Hypocentral locations of 82 earthquakes (circles) with $3 \leq m \leq 5$ used in this study. The size of each circle scales with the magnitude listed in the JMA catalogue, and the color corresponds to its hypocentral depth. The 692 Hi-net array stations are plotted as gray triangles. The waveforms recorded by station KNHH (red star) generated from an $m = 4.1$ event 05051315 (pointed by an arrow) are shown in Figure 3.

Figure 2. (a) Map view of the seismicity (circle) from the JMA catalogue around the $m = 4.1$ event 05051315. Earthquakes occurred before the mainshock are shown by open circles, and those after the mainshock are shown with color denoting the time since the mainshock. The size of each circle scales with the magnitude listed in the JMA catalogue. The large dashed red circle marks radius that are used to select foreshocks and aftershocks. (b) Cross-sectional view of the seismicity. The dashed red line marks the spatial window used in this study.

Figure 3. (a) High-pass-filtered vertical-component seismogram recorded by station KNHH for event 05021315 with $m = 4.1$. The trace is manually clipped, with the peak amplitude of the mainshock off-scale to illustrate small aftershocks. (b) Logarithm of the envelope function obtained by stacking the envelopes of the high-pass-filtered three-component seismograms. Each red circle marks a seismic phase arrival (i.e., either *P*- or *S*- wave of an event). A total of 33 events are identified by the

handpicking procedure. The blue triangle marks the amplitude level right before each event. The two green stars denote the times of event identification in the JMA catalogue. The magnitude for this sequence can be estimated using an empirical relationship $m = \log_{10}(\text{amplitude}) - 1.88$.

Figure 4. A comparison of magnitudes listed in the JMA catalogue and derived from the envelope amplitudes for events identified in the 82 sequences. The diagonal line denotes perfect correlation. The dashed line is the best-fitting regression line for magnitudes larger than 1.5.

Figure 5. Event magnitudes versus logarithmic times after (a) and before (b) the $m$ = 4.1 mainshock shown in Figures 1 and 3. Each red circle marks an event picked by hand. The green star denotes an event listed in the JMA catalogue. The black curve is the high-pass-filtered envelope function for station KNHH. The blue triangle marks the amplitude level before each event. The horizontal dashed line marked the amplitude level before the mainshock. The vertical line denotes the end time of the waveform data we have available. The increase in amplitude at $t \approx 4$ s before the mainshock is due to the mainshock first arrival.

Figure 6. Event magnitude versus logarithm of times after (a) and before (b) the 82 mainshocks. The red circles mark events picked by hand only, and the blue circles mark those picked by hands and listed in the JMA catalog. The green stars denote

events listed in the JMA catalogue. Events in the JMA catalogue with no magnitude (open stars) are assigned $m = -2.0$. A random number between −0.05 and 0.05 is added to the magnitudes for plotting purposes. The two arrows mark the time of 900 s (a) and −200 s (b) from the mainshock occurrence time when we have waveform recordings for all 82 sequences.

Figure 7. The ratio between events listed in the JMA catalogue and identified by the handpicking procedure with four different magnitude thresholds in bins of equal width in the logarithm of time. The vertical dashed line marks the time of 200 s after the mainshock.

Figure 8. (a) Cumulative (square) and non-cumulative (triangle) number of aftershocks versus magnitude for events listed in the JMA catalogue starting 2000 s after the mainshock. The solid line marks the maximum-likelihood fit for the frequency-magnitude relationship. The inverted black triangle marks the maximum curvature of the non-cumulative distribution. The dark diamond denotes the magnitude of completeness $m_c$. (b) Same as in (a) except for the handpicked events starting 200 s after the mainshock. (c) The $m_c$ value (gray dot) obtained from the pre-event noise level of each handpicked aftershock versus logarithmic time after the mainshock for all 82 sequences. The open circle denotes the magnitude below which 95% of the $m_c$ values (gray dots), or $m_{c95}(t)$, as a function of time for every 100 points. The average and standard deviation in magnitude for $m_{c95}(t)$ after 200 s, 0.21±0.18, are marked by the solid and dashed lines.

Figure 9. Seismicity rate for the 82 sequences as a function of time relative to the mainshock. The blue circle denotes the rate measured from the aftershocks in the JMA catalogue. The red plus marks the rate measured from the handpicked events after correcting for the $m_c$. The green cross and red triangle denote the foreshock seismicity rate from JMA catalogue and handpicked events, respectively. All curves have been shifted so that their $m_{c0}$ = 1.0. The solid lines mark the least- square fitting for different seismicity rate. The corresponding slopes ($p$ values) and the 95% confidence levels are marked, where $p_{HP}$, $p_{JMA}$, $p^*_{HP}$, and $p^*_{JMA}$ stands for the $p$ value for the handpicked aftershocks, aftershocks in the JMA catalogue, handpicked foreshocks, and foreshocks in the JMA catalogue, respectively. The dash line denotes a reference line with $p$ = 1. The background seismicity rate, defined as the logarithmic average of the foreshock rate $10^7$ s before the mainshock, is marked by the horizontal line.

Figure 10. (a) The measured $p$ value and the 95% confident level as a function of magnitude of completeness $m_{c0}$ for early aftershocks by handpicking (gray solid line), late aftershocks listed in the JMA catalogue (black solid line), immediate foreshocks by handpicking (gray dashed line), and foreshocks listed in the JMA catalogue (black dashed line). (b) The measured $p$ value and the 95% confident level as a function of magnitude shift for different categories.

Figure 11. (a) Aftershock rates as a function of the time since the mainshock for two groups

of sequences according their aftershock productivity (see text for description). To produce smoother curve for comparison, we use a window size of 21 points to compute the seismicity rate. The solid, dashed and dotted lines show the reference rate with $p$ = 1, 0.8, and 0.5, respectively, for comparison of slope. (b) Aftershock rates as a function of the time since the mainshock for four magnitude ranges with a 0.5 unit intervals based on the mainshock magnitude. (c) Measured $p$ values corresponding to different groups as shown in (a) and (b) for the early aftershocks by handpicking (gray circles) and late aftershocks listed in the JMA catalogue (dark triangles). The vertical bars denote 95% confidence level of the fit.

Figure 12. (a) Stacked envelope function for the 82 sequences immediately before and after the mainshocks. (b) Smoothed amplitude for foreshocks (solid gray curve) and aftershocks (solid black curve). The dashed black line denotes a least-squares fit to the data between 30 and 900 s, with a $p$ value of 0.69. The dotted gray line is generated with $p$ = 0.92 (corresponding to the aftershock decay rate at later time, as shown in Figure 9) for comparison. The origin time is chosen as the mainshock peak amplitude. An increase in amplitude at $t \approx 6$ s before the mainshock is due to the mainshock first arrival.

Figure 13. Comparison of the observed foreshock (square) and aftershock (circle) decay rates in this study. The horizontal bars mark the time range in which the least-squares fitting with $1/t^p$ is made. The vertical bars denote 95% confidence level of the fit.

Figure 14. Seismicity rate (black line) observed in this study, and a fit (red line) by the rate-and-state model assuming a Gaussian stress distribution.

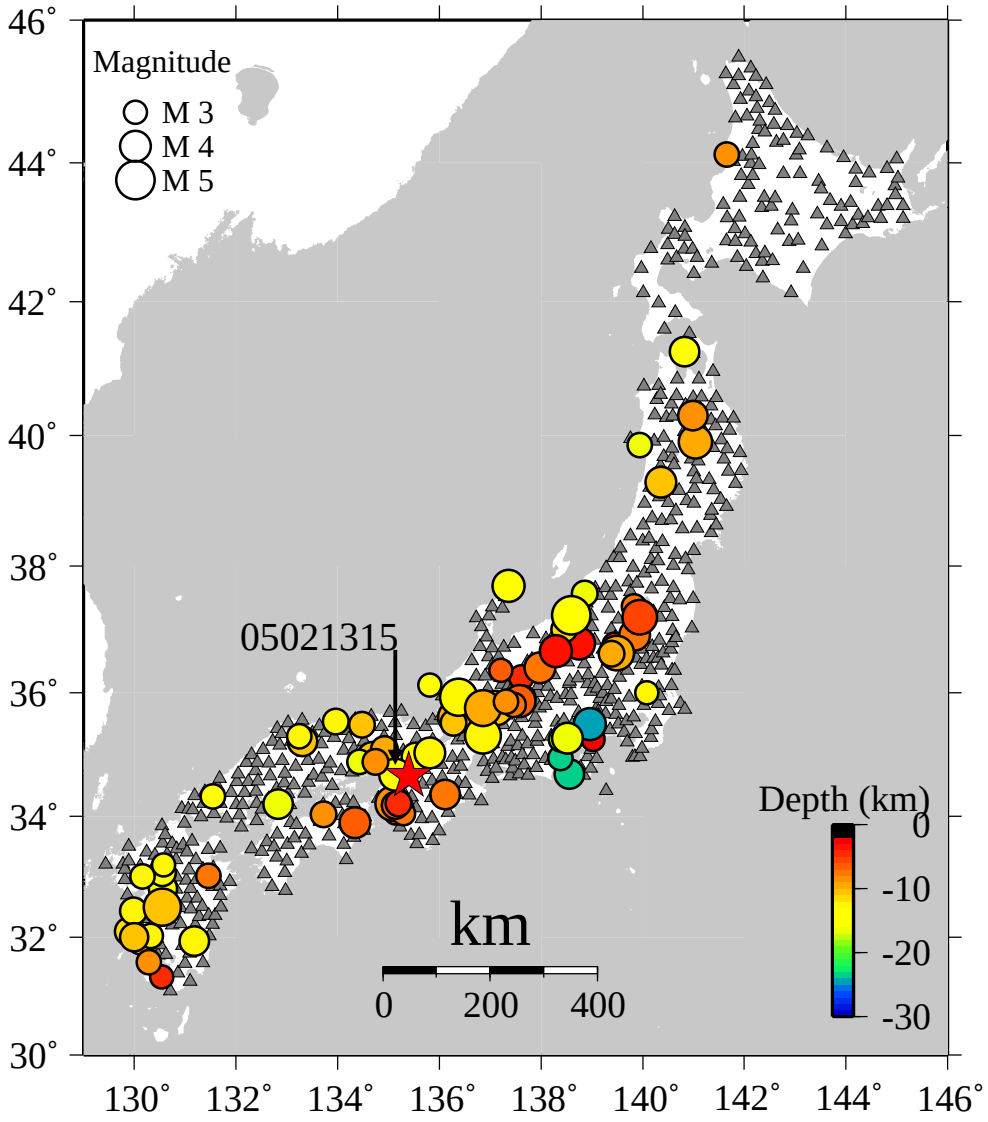
Magnitude
M 3
M 4
M 5
05021315
km
0
200
400
Depth (km)
0
-10
-20
-30
46˚
44˚
42˚
40˚
38˚
36˚
34˚
32˚
30˚
130˚
132˚
134˚
136˚
138˚
140˚
142˚
144˚
146˚

Figure 1

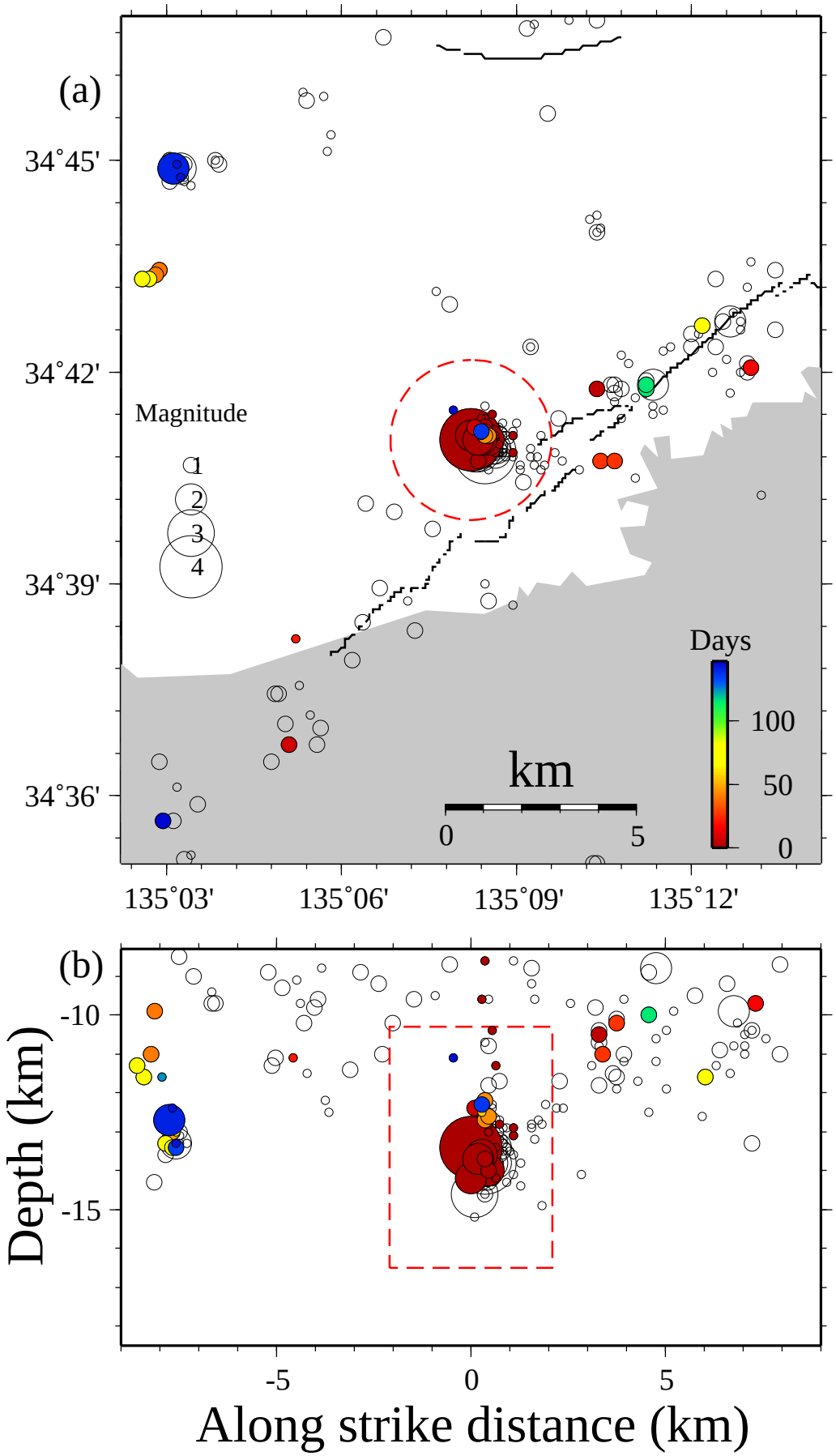
(a)
34˚45'
34˚42'
34˚39'
34˚36'
Magnitude
1
2
3
4
Days
100
50
0
km
0
5
135˚03'
135˚06'
135˚09'
135˚12'
(b)
-10
-15
Depth (km)
-5
0
5
Along strike distance (km)

Figure 2

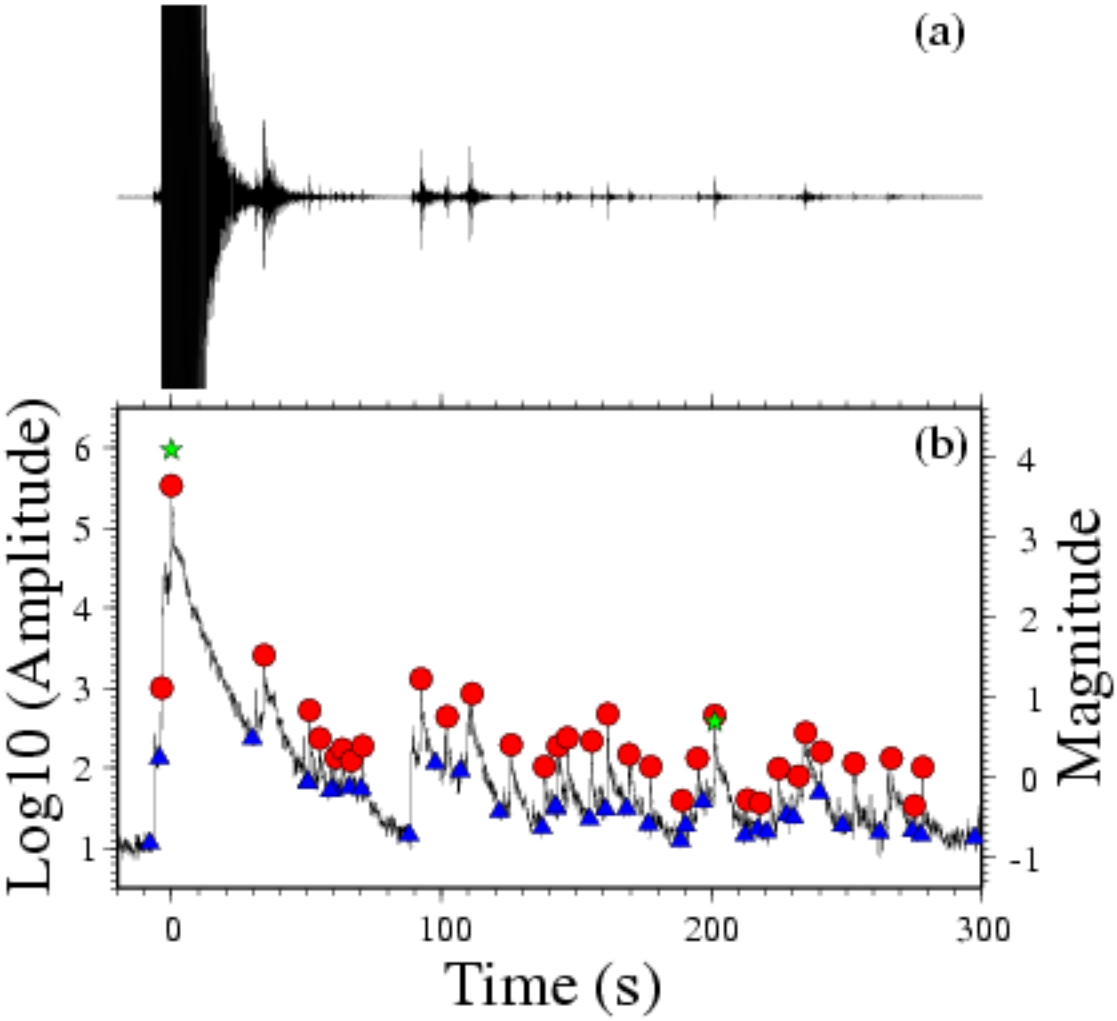
(a)
(b)
Log10 (Amplitude)
Magnitude
Time (s)
0
100
200
300
1
2
3
4
5
6
-1
0
1
2
3
4

Figure 3

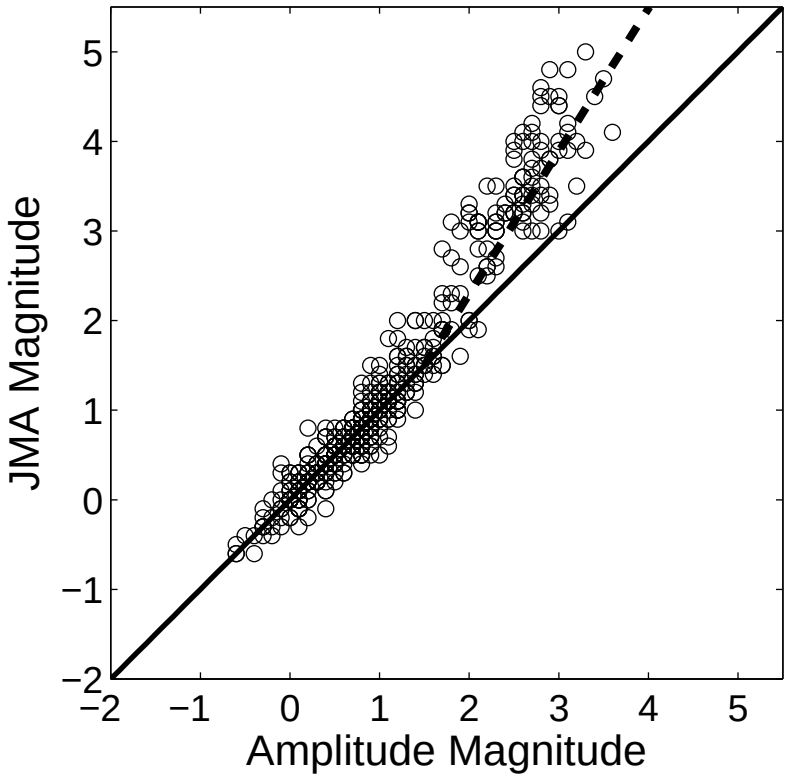


Figure 4

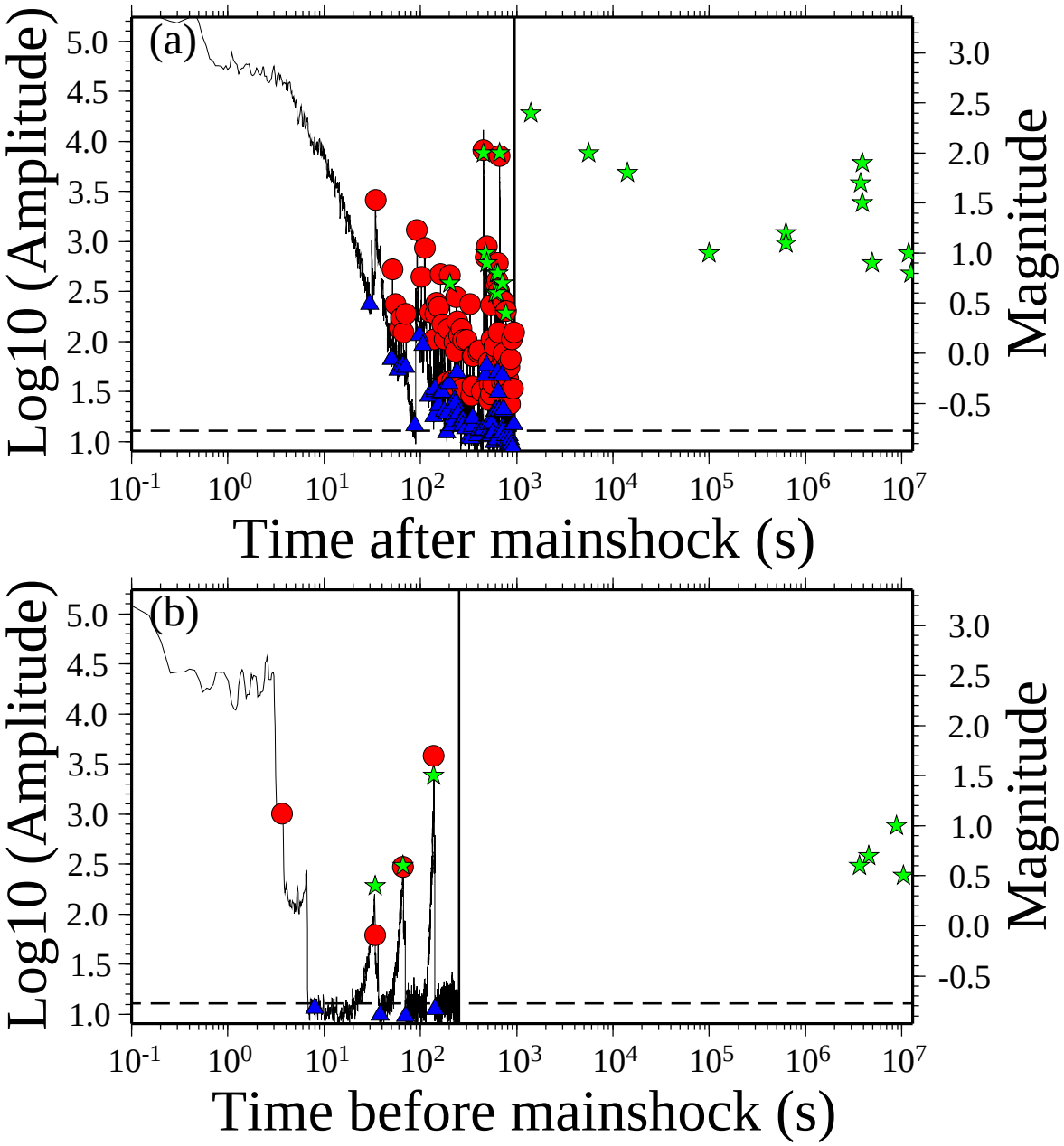
(a)
Log10 (Amplitude)
Magnitude
Time after mainshock (s)
(b)
Log10 (Amplitude)
Magnitude
Time before mainshock (s)

Figure 5

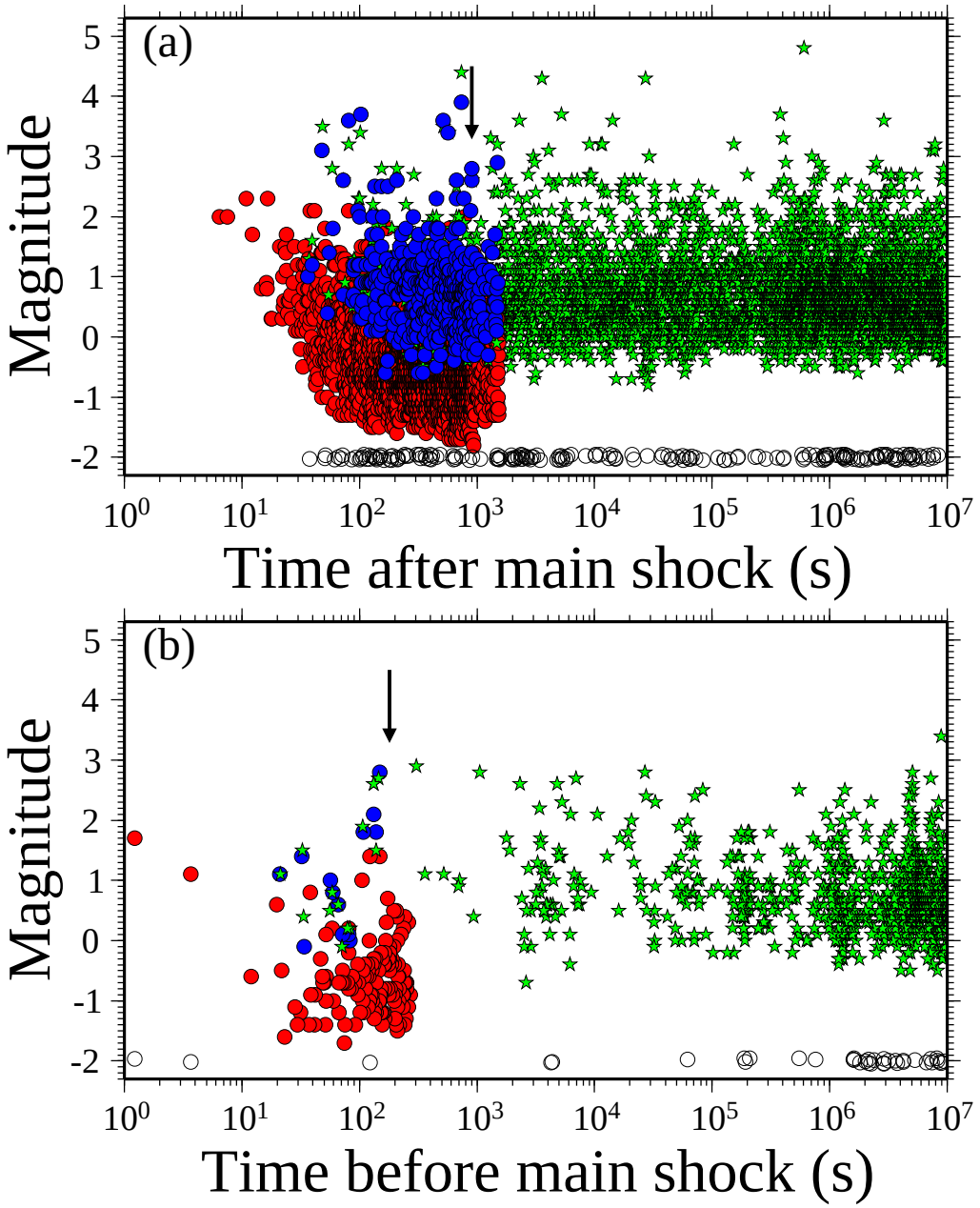
(a)
Magnitude
Time after main shock (s)
(b)
Magnitude
Time before main shock (s)

Figure 6

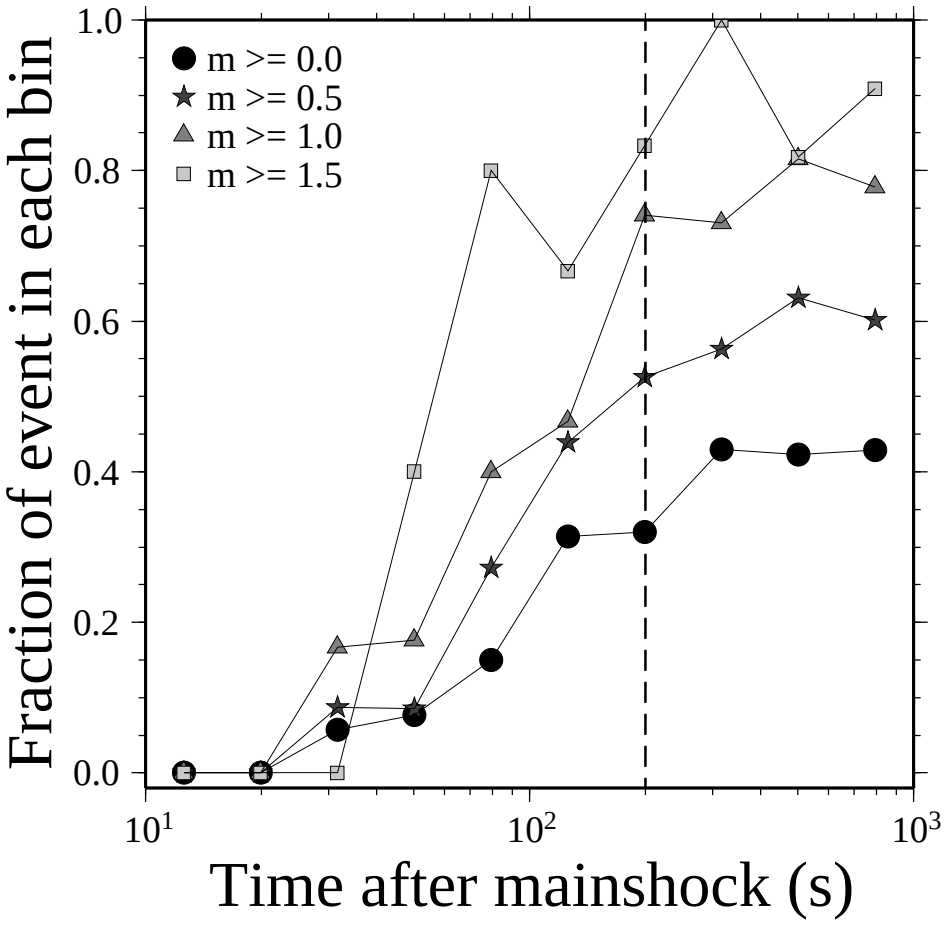
m >= 0.0
m >= 0.5
m >= 1.0
m >= 1.5
Fraction of event in each bin
Time after mainshock (s)
1.0
0.8
0.6
0.4
0.2
0.0
10^1
10^2
10^3

Figure 7

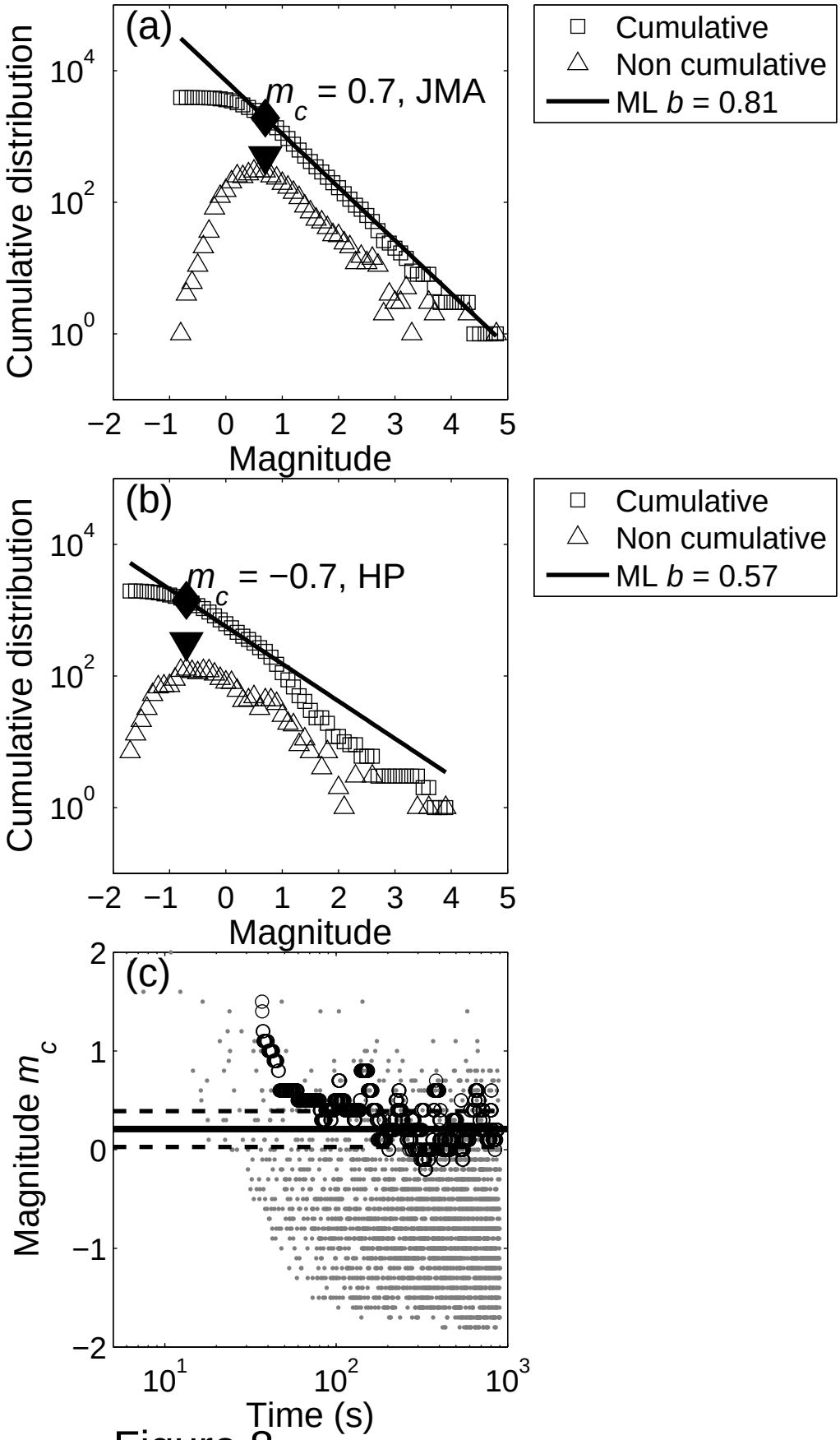
(a)
$m_c$ = 0.7, JMA
Cumulative
Non cumulative
ML $b$ = 0.81
Cumulative distribution
Magnitude
(b)
$m_c$ = −0.7, HP
Cumulative
Non cumulative
ML $b$ = 0.57
Cumulative distribution
Magnitude
(c)
Magnitude $m_c$
Time (s)

Figure 8

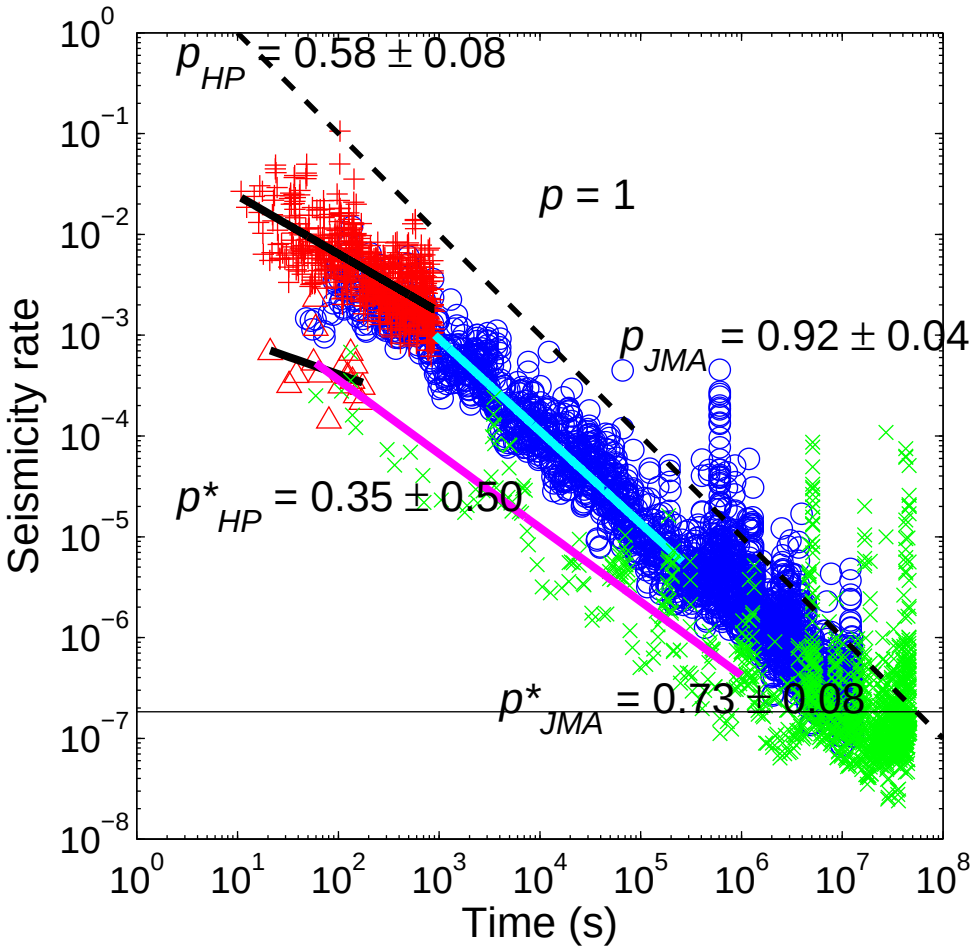
$p_{HP}$ = 0.58 ± 0.08
$p$ = 1
$p_{JMA}$ = 0.92 ± 0.04
$p^*_{HP}$ = 0.35 ± 0.50
$p^*_{JMA}$ = 0.73 ± 0.08
Seismicity rate
Time (s)
$10^0$
$10^{-1}$
$10^{-2}$
$10^{-3}$
$10^{-4}$
$10^{-5}$
$10^{-6}$
$10^{-7}$
$10^{-8}$
$10^0$ $10^1$ $10^2$ $10^3$ $10^4$ $10^5$ $10^6$ $10^7$ $10^8$

Figure 9

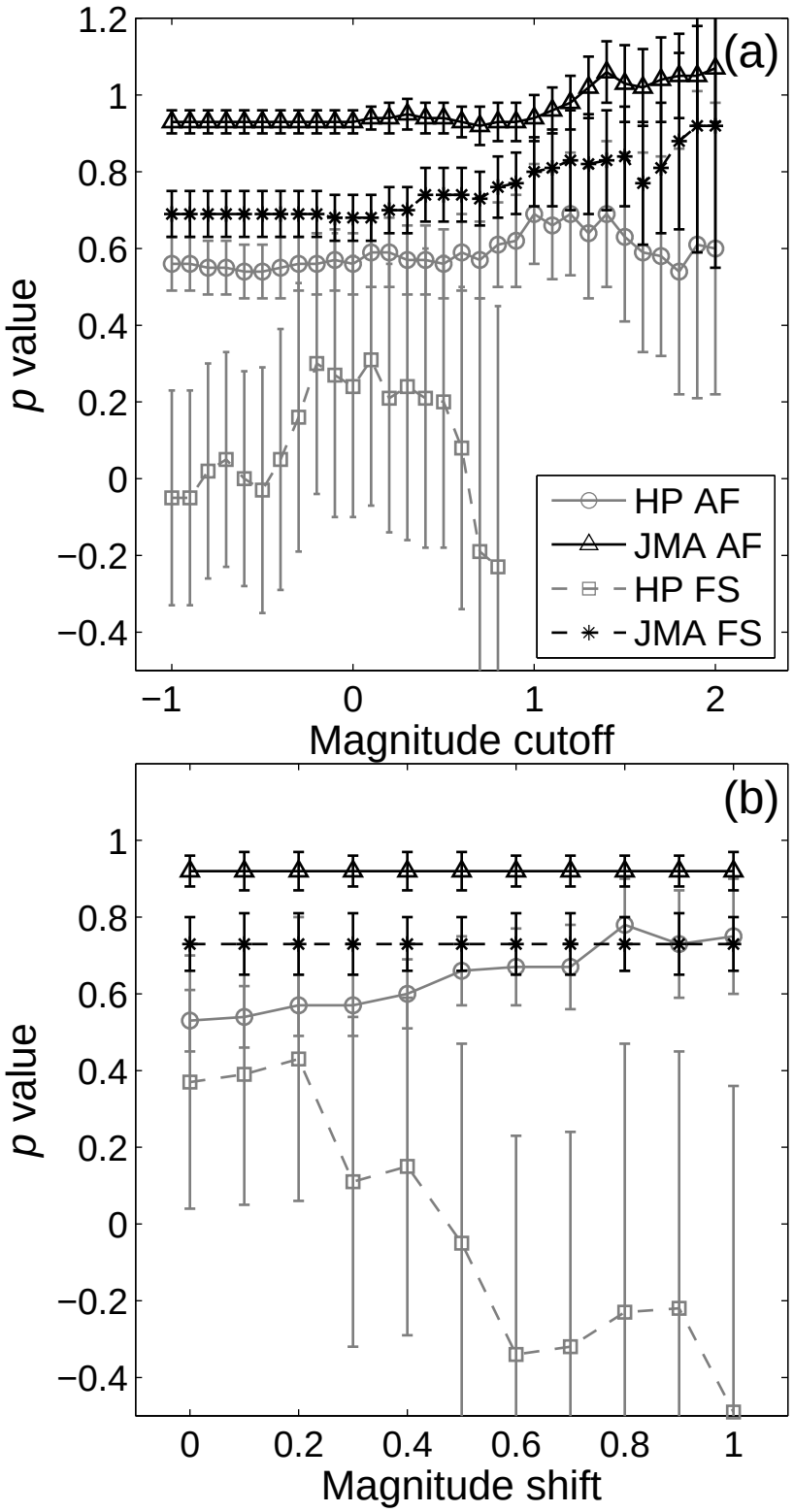
(a)
p value
Magnitude cutoff
HP AF
JMA AF
HP FS
JMA FS
(b)
p value
Magnitude shift

Figure 10

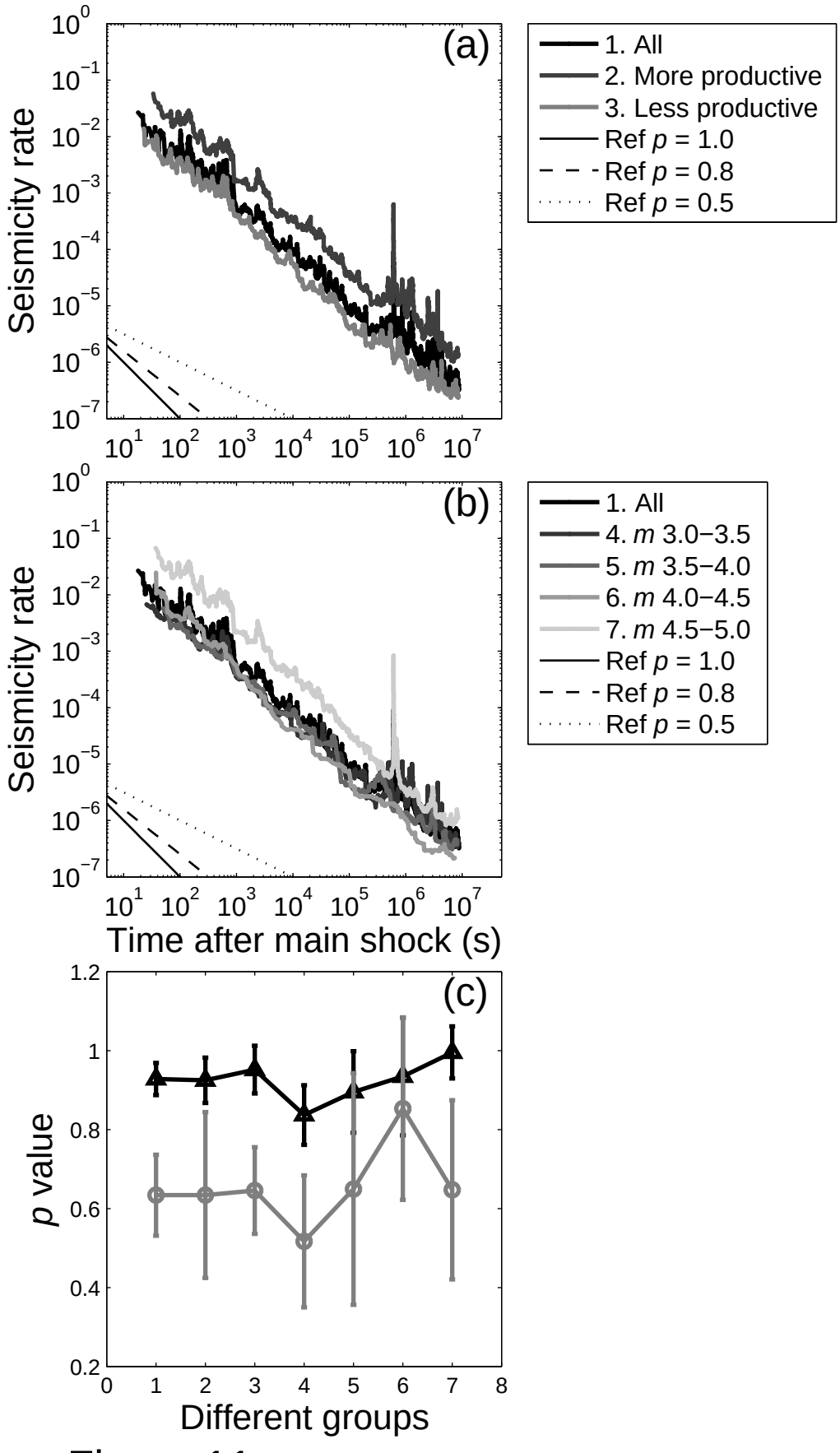
(a)
Seismicity rate
1. All
2. More productive
3. Less productive
Ref p = 1.0
Ref p = 0.8
Ref p = 0.5
(b)
Seismicity rate
1. All
4. m 3.0−3.5
5. m 3.5−4.0
6. m 4.0−4.5
7. m 4.5−5.0
Ref p = 1.0
Ref p = 0.8
Ref p = 0.5
Time after main shock (s)
(c)
p value
Different groups

Figure 11

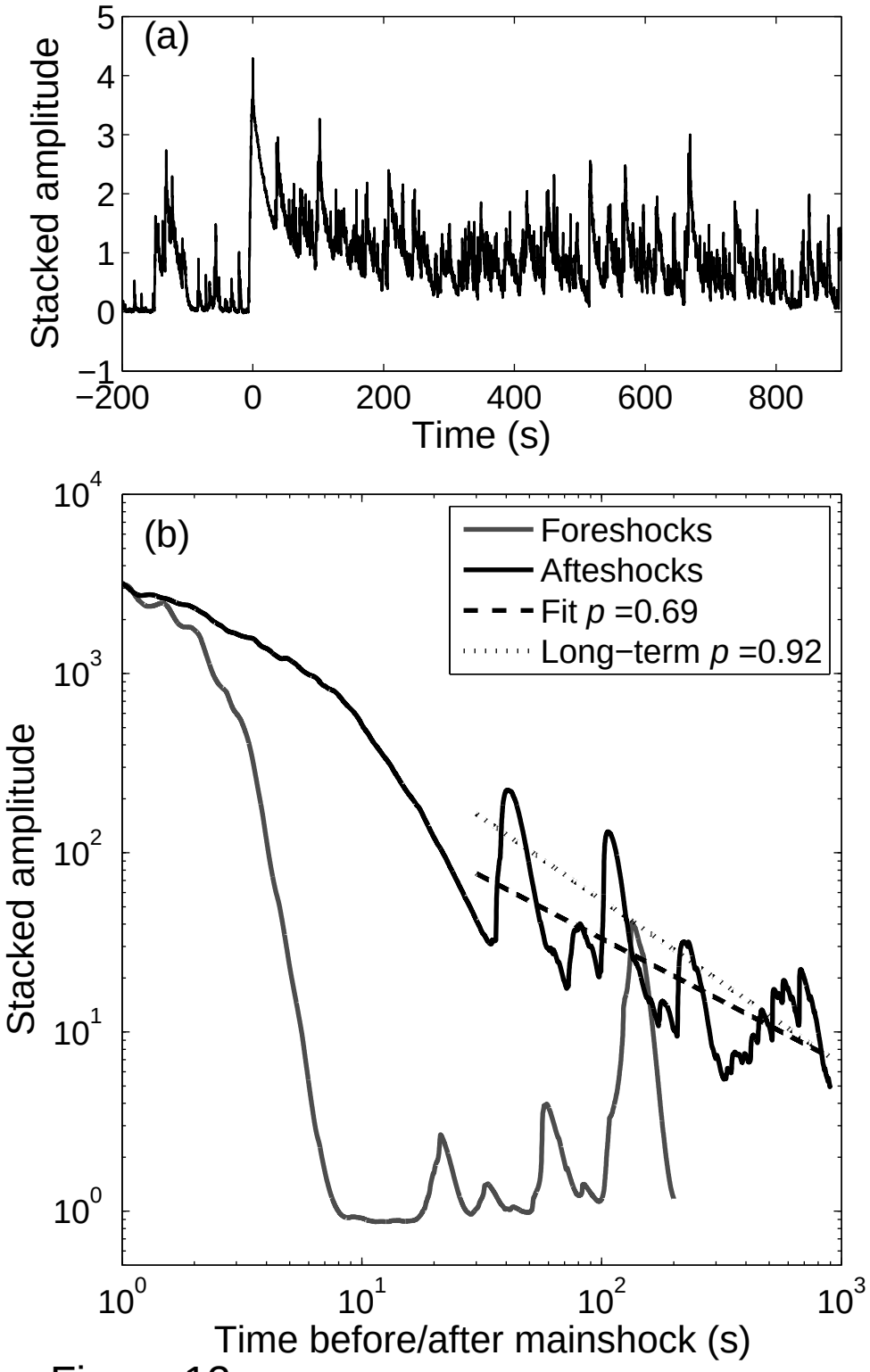
(a)
Stacked amplitude
Time (s)
(b)
Foreshocks
Afteshocks
Fit p =0.69
Long−term p =0.92
Stacked amplitude
Time before/after mainshock (s)

Figure 12

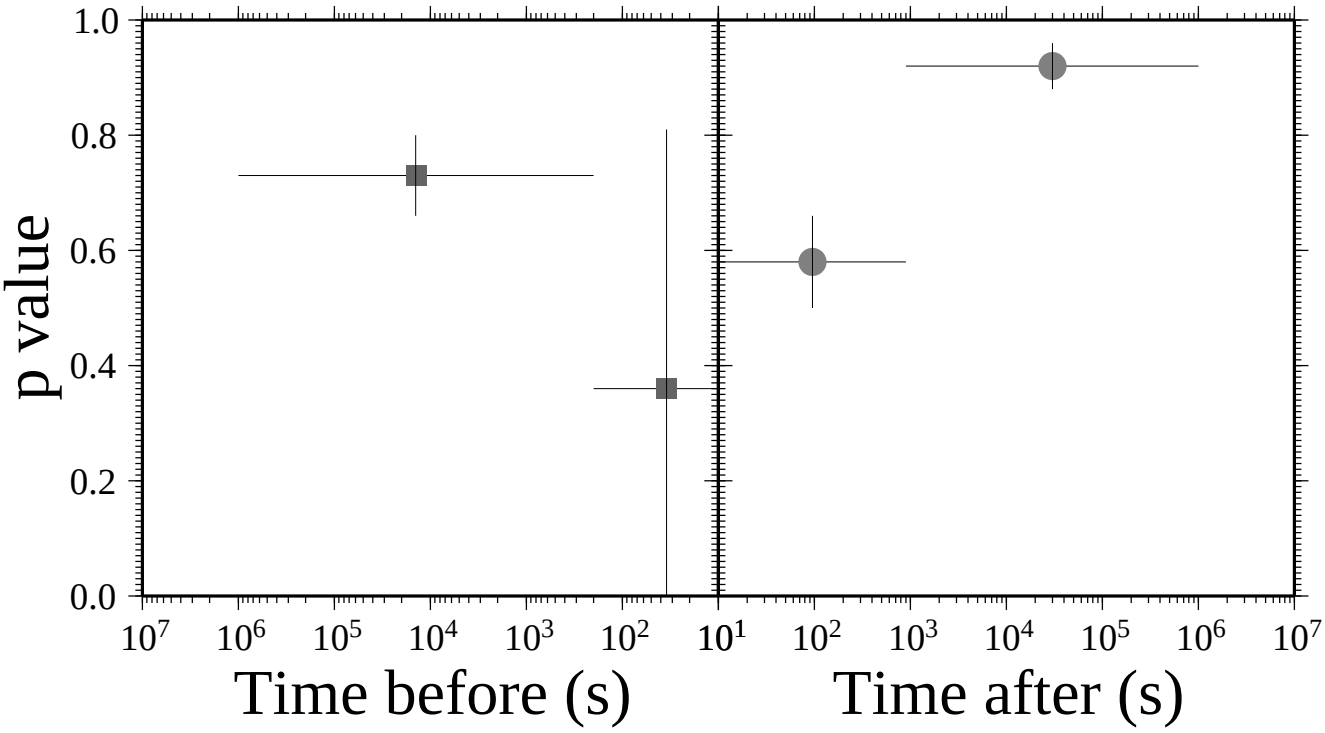
1.0
0.8
0.6
0.4
0.2
0.0
p value
$10^7$ $10^6$ $10^5$ $10^4$ $10^3$ $10^2$ $10^1$ $10^2$ $10^3$ $10^4$ $10^5$ $10^6$ $10^7$
Time before (s)
Time after (s)

Figure 13

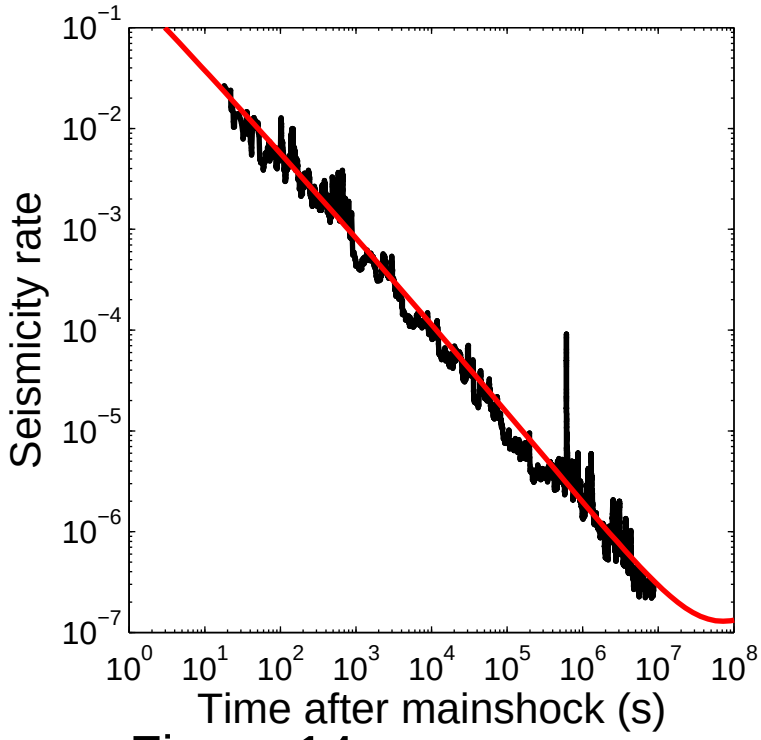
Seismicity rate
$10^{-1}$
$10^{-2}$
$10^{-3}$
$10^{-4}$
$10^{-5}$
$10^{-6}$
$10^{-7}$
$10^{0}$ $10^{1}$ $10^{2}$ $10^{3}$ $10^{4}$ $10^{5}$ $10^{6}$ $10^{7}$ $10^{8}$
Time after mainshock (s)

Figure 14